DEVELOPMENT OF A MULTIPHOTON PHOTOACOUSTIC MICROSCOPE

A Dissertation

by

RYAN LYNN SHELTON

Submitted to the Office of Graduate Studies of
Texas A&M University
in partial fulfillment of the requirements for the degree of

DOCTOR OF PHILOSOPHY

Approved by:

Chair of Committee,	Brian E. Applegate
Committee Members,	Duncan J. Maitland
	Dong H. Son
	Alvin T. Yeh
Head of Department,	Gerard L. Coté

December 2012

Major Subject: Biomedical Engineering

ABSTRACT

Cellular/subcellular imaging of biological tissue is an important tool for understanding disease mechanisms. Many current techniques for subcellular absorption contrast imaging, such as two-photon excited fluorescence (TPEF), require exogenous contrast agents to gain access to many naturally occurring biomolecules. Non-fluorescent biomolecules must have a fluorescent marker (tag) chemically bound in order to be observed by TPEF. Contrast agents and markers, while effective, are not an optimal solution because they can change the local environment in the biological system and require FDA approval for human use. Photoacoustic microscopy (PAM) is an imaging modality with high endogenous absorption contrast and penetration depth due to its ability to detect acoustic waves, which are attenuated much less than light in tissue. However, this technique suffers from poor axial resolution, precluding it from consideration for subcellular imaging.

This manuscript describes the author's efforts to improve the axial resolution of traditional PAM by merging it with pump-probe spectroscopy. Pump-probe spectroscopy is a non-linear optical technique that exploits a physical process called transient absorption, providing spatial resolution equivalent to two-photon microscopy and access to molecular-specific traits, such as the ground state recovery time and transient absorption spectrum. These traits provide molecular contrast to the imaging technique, which is highly desirable in a complex, multi-chromophore biological system.

In this manuscript, a novel technique called transient absorption ultrasonic

microscopy (TAUM) is designed and characterized in detail. A second-generation TAUM system is also described, which improves speed and sensitivity of TAUM by up to 1000-fold. This system is validated by collecting volumes of red blood cells in blood smears and tissue samples. These results constitute the first time single cells have been fully resolved using a photoacoustic microscope. Finally, the TAUM system is modified to measure chromophore ground state recovery times. This technique is validated by measuring the recovery time of Rhodamine 6G, which matches well with published values of the fluorescence lifetime. Recovery times of oxidized and reduced forms of hemoglobin are also measured and shown to statistically differ from one another, suggesting the possibility of subcellular measurements of oxygen saturation in future iterations of TAUM.

DEDICATION

To my dad, the science teacher.

ACKNOWLEDGEMENTS

I would like to thank my committee chair, Dr. Applegate, for the time he has invested in me over the past few years. His role has been vital in making my graduate school experience as rewarding as it has been for me. I would also like to thank my committee members, Dr. Maitland, Dr. Son, and Dr. Yeh, for their guidance and support throughout the course of this research.

There are several people that were essential to the success of this research, whether contributing by hands-on lab work, helpful discussions, or shared resources. For this, I would like to thank Scott Mattison, David Tagawa, Kalyanramu Vemishetty, Sarah Ritter, Holly Gibbs, Bilal Malik, Brian Cummins, and Sara Mashoof.

Thanks also go to my friends and colleagues in the biomedical engineering department for making my time at Texas A&M University a great experience. My graduate career would have been much more difficult (and boring) without their constant support.

Finally, I would like to say thanks to my wife and son for putting up with the long, sometimes abnormal hours and for supporting me in whatever I do. I truly could not have accomplished all that I have without their love and support. I would also like to thank my mom, dad, and siblings for their love and support.

TABLE OF CONTENTS

Page

LIST OF FIGURES

Page

CHAPTER I

INTRODUCTION AND LITERATURE REVIEW

Molecular imaging

High-resolution molecular imaging has established itself as an important tool for research in biology and biochemistry [1-5]. Imaging the molecular content in a biological sample with subcellular resolution provides insights into disease from an early stage, leading to a better understanding of disease mechanisms. High-resolution optical molecular imaging extracts comparable information to that obtained from histopathological evaluation of tissue sections, but does not require a tissue biopsy [6-9]. Tissue biopsy, while highly informative and the current gold standard, cannot evaluate dynamic molecular processes, since the examined tissue is dead. Additionally, tissue biopsy suffers from separation and cracking artifacts that occur during tissue preparation. High-resolution optical molecular imaging stands poised to augment or eventually replace tissue biopsy for accessible anatomy because it is non-invasive, highly sensitive and boasts excellent molecular specificity [10, 11].

Among the most widely used three-dimensional optical molecular imaging techniques are confocal fluorescence microscopy [12, 13] and multi-photon fluorescence microscopy [14-16]. Both techniques provide subcellular resolution, but since these modalities collect signal via fluorescence, they are limited to a very small pool of endogenous fluorophores. For all other endogenous targets, exogenous contrast agents or genetic modification in the form of fluorescent proteins must be employed. While

exogenous contrast agents work well in *ex vivo* and animal studies, they are not ideal for studies in humans, since it can be very difficult to obtain FDA approval for such agents. Additional optical molecular imaging techniques include other multi-photon techniques, such as second and third harmonic generation [17, 18] and sum frequency generation [19]. Second harmonic generation has been used extensively for imaging collagen, but the noncentro-symmetric requirement of SHG severely limits its pool of accessible chromophores. Coherent Anti-Stokes Raman Scattering (CARS) has been a very hot topic the past several years. CARS inherently measures vibrational resonances, which makes it widely applicable across a large range of chromophores. CARS has been shown to be successful as a high resolution molecular imaging modality [20] with similar resolution to multi-photon fluorescence microscopy. However, CARS is most efficient in transmission geometry and has a limited penetration depth due to the excitation wavelengths, which are typically in the visible spectrum.

Pump-probe (transient absorption) spectroscopy

Pump-probe spectroscopy is a well-established tool in molecular physics for measuring the spectrum and dynamics of molecular species that exhibit low fluorescence quantum yield. In this technique, a pump beam and a probe beam are incident on the chromophore. On a molecular level, interaction with the pump radiation induces changes in molecular state populations. The probe interrogates these population changes and reports via a pump dependent change in the probe attenuation. If the pump is amplitude modulated, the modulation will be transferred to the probe. Nominally, the probe must

be delayed in time relative to the pump. This phenomenon is illustrated in a 2-level energy diagram in Figure 1, where the x-axis corresponds to increasing time and the y-axis corresponds to increasing energy. As shown in the diagram, a pump pulse first drives a percentage of the ground state electrons into a higher energy state. The probe pulse then drives a percentage of the remaining electrons into the higher energy state. The percentage of electrons driven by each pulse determines the amount of absorption that occurs due to each pulse. With this in mind, observing the probe signal (either by looking at remaining transmitted light or looking at a subsequent process such as fluorescence or photoacoustic emission) with and without the presence of the preceding pump pulse provides insight into the electron dynamics of the molecule.

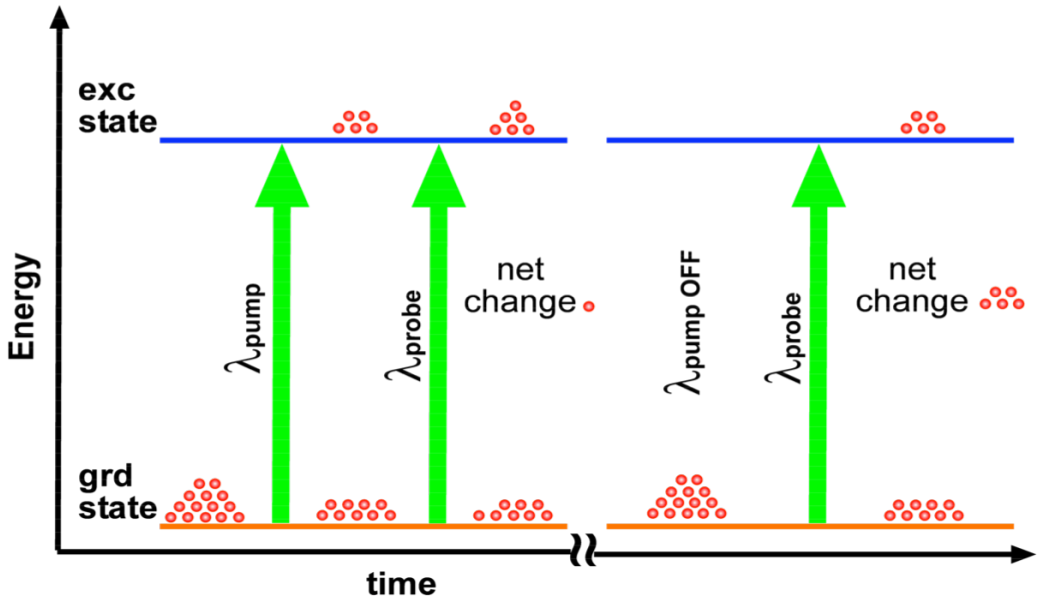

Figure 1. Schematic of an energy level diagram illustrating the transient absorption process. The "pump on" condition is shown on the left side of the diagram, while the "pump off" condition is shown on the right side of the diagram. Note the difference in the "net change" for each case. This difference is the result of the transient absorption process.

If the probe signal is measured as a function of the interpulse pump-probe delay, the signal should map out an exponential that decays at a characteristic time corresponding to the time it takes the molecular state population to return to equilibrium. This time is often referred to as the ground state recovery time of the molecule. Pump-probe spectroscopy has recently been harnessed for high-resolution molecular imaging. Hemoglobin [21] and melanin [22], both of which do not give off observable fluorescence, were imaged using this technique. However, the imaging depth is currently restricted to < 100 μm and trans-illumination geometry is used. This technique is the closest competitor to the technology developed by the author in this manuscript.

It is important to note that there are many possible electronic state couplings that may be measured with pump-probe techniques. Figure 2 shows a schematic diagram listing many possible excitation and relaxation pathways. Depending on the wavelength of the pump and probe pulses, as well as the allowable transitions in the molecule, each of these pathways (simultaneously, in some cases) may be measured using pump-probe techniques.

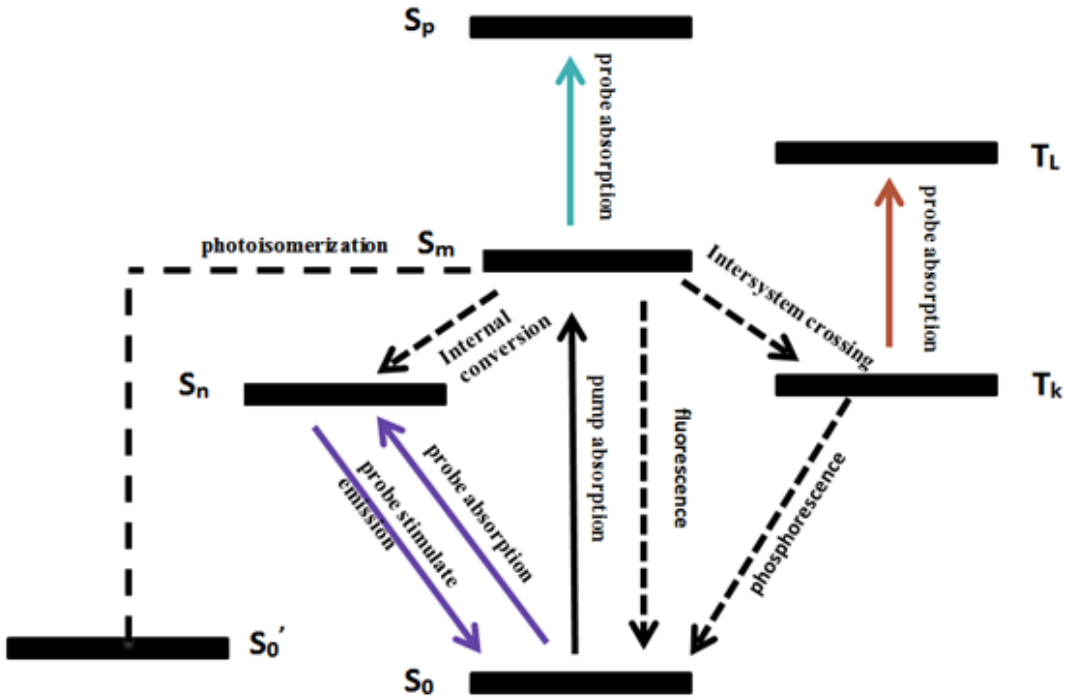

Figure 2. Multilevel energy level diagram showing various possible transitions accessible through pump-probe techniques.

Photoacoustic microscopy

Photoacoustic microscopy (PAM) is an absorption contrast imaging technique that has seen rapid growth in recent years. PAM harnesses the photoacoustic effect; in which pulsed optical excitation induces molecular vibrations in a chromophore, leading to rapid thermoelastic expansion and the emission of a pressure wave. The pressure wave can then be detected with an ultrasound transducer, providing depth information about the chromophore through the time-of-flight measurements of the recorded ultrasound signal. One of the main benefits of photoacoustic imaging is the fact that the signal is generated through vibrational relaxation of the excited molecules, not radiative

transitions such as fluorescence and stimulated emission. This results in a much larger pool of chromophores that can be reached by photoacoustic imaging, since for the vast majority of chromophores, biological or otherwise, the most probable relaxations are non-radiative. For this reason, PAM can image many biological chromophores that are not accessible to other absorption contrast techniques unless exogenous contrast agents, such as fluorescent tags, are employed. Heme proteins, melanin, nanoparticles, transgenic proteins and fluorescent dyes are all equally viable targets for PAM.

Although any chromophore with sufficient absorption is a potential imaging target for PAM, there are specific biomolecules that are investigated heavily in photoacoustic research. These biomolecules include hemoglobin [23], melanin [24], and DNA/RNA [25]. All of these biomolecules exhibit very poor fluorescence, which make them very attractive targets for PAM. Exogenous contrast agents include gold nanoparticles [26] and fluorescent dyes [27], both of which exhibit very strong photoacoustic signals.

Regarding spatial resolution, one of the primary benefits that photoacoustic imaging boasts in tomographic implementations becomes the primary drawback in microscopic implementations. Photoacoustic tomography (PAT) is well-known for its ability to maintain good spatial resolution up to centimeters in depth in tissue. The spatial resolution in PAT is largely determined by the rate at which the transducer converts pressure into voltage. This parameter is heavily dependent on the bandwidth of the piezo crystal. This dependence of spatial resolution on the transducer bandwidth is a boon to PAT systems, because not only does it result in admirable resolutions (~ 10s –

100s of μm) deep in tissue, but it also provides scalability depending on the goals of the imaging system. If higher resolution at shallower depths is desired, the tranducer bandwidth can simply be increased with no other changes to the imaging system. This is a great boon to a PAT system, but becomes a fundamental limitation when scaled down to microscopic length scales. The point spread function of PAM is limited by the ultrasound transducer bandwidth in the axial dimension (similar to PAT) and either the focusing of the ultrasound transducer or the focusing of the excitation beam in the transverse dimension, depending on which implementation of PAM is used. In the former, unfocused light is shone on the sample and the signal localization is achieved solely through the focused transducer parameters. This results in axial and transverse resolutions in the 10s of microns at penetration depths up to centimeters [28]. In the latter, which was pioneered by Dr. Lihong Wang in 2008 and coined "optical resolution PAM" (OR-PAM) [29], focused optical excitation is used to localize signal in the transverse dimension, while the transducer bandwidth still governs the localization of signal in the axial dimension. This technique yields similar axial resolutions, but improves the transverse resolution to match other high-resolution optical imaging techniques.

Since the axial resolution of PAM is proportional to the bandwidth of the ultrasonic transducer, better axial resolution can be achieved with larger bandwidth detectors. However, as the frequency of the acoustic wave increases, the attenuation of that wave in tissue also increases. The acoustic attenuation in water, which is a good approximation of tissue attenuation, is ~0.15 dB/mm at 25 MHz and ~2 dB/mm at 100

MHz [30]. In order to achieve axial resolution on par with nonlinear microscopy (~1.5 μm), a bandwidth of 1 GHz would be required. At 1 GHz the acoustic attenuation in water is ~115 dB/mm. This large attenuation at high frequencies restricts the maximum transducer bandwidth to roughly 100 MHz in order to maintain an imaging depth of at least 500 μm. This restriction on bandwidth places a fundamental limit on the axial resolution of PAM techniques. A transducer with a bandwidth of 100 MHz will provide ~ 15 μm axial resolution. While this is sufficient for mapping out most vasculature, which is a primary application for PAI, it has proven to be a significant barrier preventing PAM from resolving cells in multiple axial planes or acquiring three-dimensional datasets of cellular and subcellular structures.

In the reported work, photoacoustic microscopy is merged with pump-probe spectroscopy to introduce optical resolution to PAM in all dimensions. The marriage of these technologies has the added benefit of providing increased molecular contrast and specificity to PAM. The result is a submicron resolution molecular imaging modality sensitive to all optical absorbers with a potential imaging depth of > 500 μm.

Field programmable gate arrays

As new technology is developed and imaging systems are pushed faster and faster, image processing becomes a real concern. One of the primary requirements for an imaging system to be considered for clinical use is whether it has real time (or quasi-real time) image output. Hours or even minutes of post processing required before an acquired image is displayed causes problems when a decision needs to be made based

off of the information gleaned from the image. This is where field programmable gate arrays (FPGAs) have made their introduction into medical imaging. FPGAs consist of billions of transistors that make up configurable logic blocks (CLBs) capable of complex mathematics, digital filtering, and high-speed synchronization. The FPGA logic blocks are interconnected with a programmable wiring mesh that allows complete reconfigurations of the signal routing, providing significant flexibility for a variety of applications. Figure 3 shows an example of how a desired function (F in the figure) might be implemented in the wiring mesh of a FPGA.

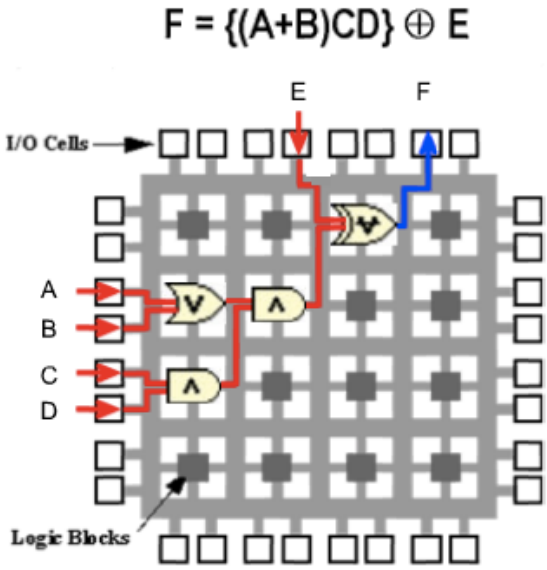

Figure 3. Drawing depicting a possible routing configuration on a field programmable gate array. The function, F, is implemented by routing the input signals (A, B, C, D, and E) to the appropriate logic blocks to generate the proper output at F. (Image openly available at http://www.ni.com.)

Serial processors, such as those found in personal computers, excel at running operating systems and performing sequential tasks; however, they typically struggle with high performance computation and simulation. This is because they are made to be versatile, performing adequately when running a wide array of applications. Parallel processing, such as the processors found in graphics processing units (GPUs) and FPGAs can be much more efficient when it comes to computation and simulation because they can run many simultaneous tasks without any performance decrease from increased load. Any algorithm that can be parallelized (such as the fast Fourier transform) will see great benefits in execution time when executed on an FPGA.

FPGAs have found use in many imaging applications, including optical coherence tomography (OCT) [31], fluorescence lifetime imaging (FLIM) [32], confocal microscopy [33], ultrasound imaging [34], and magnetic resonance imaging [35]. Any imaging system that has significant image processing or strict synchronization requirements stands to benefit from FPGA technology. As is detailed hereafter, TAUM requires a significant amount of processing including a large array fast Fourier transform, which makes this technology an excellent candidate for FPGA implementation.

CHAPTER II

OFF-AXIS PHOTOACOUSTIC MICROSCOPY*

Initial prototype

This section of Chapter II introduces the technique of off-axis photoacoustic microscopy (OA-PAM) and describes the methods and results of the initial prototype system. OA-PAM forms the foundation of the multiphoton photoacoustic microscope discussed in later chapters.

Introduction

Photoacoustic microscopy (PAM) is a hybrid optical and ultrasonic modality that combines optical absorption contrast with optically limited lateral resolution and ultrasonic-limited axial resolution. PAM is well suited to mapping microvasculature and other micron scale structures containing strongly absorbing tissue chromophores. PAM is based on the photoacoustic effect, in which pulsed, incident light is absorbed, causing a pressure wave to emit from the absorber due to thermal expansion. These pressure waves can then be detected using a focused ultrasonic transducer to provide depth-encoded, absorption contrast signals [36].

The ability of PAM to resolve the morphology of the microvasculature deep inside living tissue currently has few rivals. With resolutions approaching the size scale

---

*Part of this chapter was reprinted with permission from "Off-axis photoacoustic microscopy" by R. L. Shelton and B. E. Applegate, 2010. *IEEE Transactions on Biomedical Engineering*, 57 (8), 1835-1838, Copyright 2010 by IEEE.

of capillaries, it has the potential to be the method of choice for interrogating the microvasculature. At this stage in the development of PAM, it is largely limited to laboratories specializing in photoacoustic imaging, in part due to the challenge of implementing the co-axial designs currently in the literature.

Over the past decade, photoacoustic microscopy has emerged as a high-contrast imaging modality with applications primarily in the field of biological imaging. PAM has been used to image acute thermal burns 3 mm deep in tissue in order to demarcate burn margins [37]. It has been used to image microvasculature deep beneath the tissue surface, for monitoring tumor angiogenesis [24, 38]. Gold nanoshells have been imaged, demarcating the boundaries of tumors in the rat brain [39]. Other implementations of PAM include a dark-field design [40] which achieved an estimated lateral and axial resolution of 45 μm and 15 μm, respectively, and a bright field design [29] using a similar 100 MHz bandwidth ultrasonic transducer which achieved lateral and axial resolutions of 5 μm and 15 μm, respectively.

Conventional PAM systems, such as the systems mentioned above, use a co-axial configuration for light delivery and ultrasonic detection [24, 29, 37]. A co-axial configuration requires custom light and acoustic optics that allow the light and pressure waves to travel the same path. We propose and demonstrate a PAM system design with off-axis ultrasonic detection. Off-axis detection enables the separation of the optical illumination and ultrasonic detection paths. Readily available, high quality optics and ultrasonic transducers may then be used to construct a photoacoustic microscope. An additional benefit of off-axis detection is that chromophores excited outside the

numerical aperture of the acoustic lens will not be detected, providing a quasi dark-field. The price of off-axis detection is a reduction in axial resolution. An ultrasonic detector capable of 15 μm axial resolution with a co-axial geometry would be reduced to 21 μm with off-axis detection at a 45º angle.

Methods and materials

The off-axis PAM system employed a Q-switched, 1064 nm, DPSS laser (SPOT 20-355, Elforlight), frequency tripled to 355 nm. Laser pulses (pulse duration ~ 1.5 ns, repetition rate = 1 kHz) were focused to ~26 μm by underfilling the aperture of a 0.3 NA objective lens (CFI W Plan Fluor 10X/.30 3.5 mm WD, Nikon). The corresponding depth of focus was 3 mm. The laser pulse energy directly after the objective lens was measured to be 700 nJ. The photoacoustic signals were collected using a 6 MHz, focused ultrasonic transducer (V310-SU, Olympus NDT), with a 6 mm element size, 80% (-6 dB) bandwidth and a numerical aperture of 0.23. The ultrasonic transducer was fixed at a 45º angle to the optical axis, as shown in Fig. 1. The resulting photoacoustic signal from the transducer was then amplified through a radio frequency amplifier (ZFL-500LN, Mini-Circuits), providing ~13 dB total amplification. The amplified signal was digitized with a high-speed digital oscilloscope (DPO-7254, Tektronix).

An automated micro-stepping stage (M-562, Newport Corp.) was employed to collect two-dimensional images and three-dimensional volumes. Custom software synchronized the micro stepping of the stage and the acquisition of data from the

oscilloscope for the collection of volumes and cross-sections. The data was then stored as photoacoustic B-scan (vertical cross-sectional) images.

The short excitation wavelength and ultrasonic transducer bandwidth used for these proof-of-principle experiments was not ideal for most biomedical imaging applications; however, they are adequate to demonstrate the salient features of the off-axis PAM design.

There are several consequences to using off-axis detection. For co-axial detection, converting the time dependent signal from the detector to axial distance is accomplished by multiplication with the sound velocity in tissue (1.5 μm/μs). However, if the detector is moved off-axis by an angle θ relative to the optical axis (45º in Figure 4), the distance traveled in the axial dimension (z) is the measured distance traveled (z') divided by the projection of z onto z', i.e.

$$z = \frac{z'}{\cos\theta} \tag{1}$$

The axial resolution is similarly affected. Nominally, the axial resolution (FWHM) of an ultrasonic transducer can be calculated by dividing the material sound velocity (v) by the transducer bandwidth (BW). Combining this relationship with the angle dependence of z noted above yields the axial resolution of an Off-Axis photoacoustic microscope:

$$Axial\ resolution = \frac{v}{\mathrm{BW}\cos\theta} \tag{2}$$

Clearly, the highest resolution is achieved in a coaxial geometry ($\theta = 0$). At 30º and 45º there is a 15% and 41% reduction in resolution, respectively.

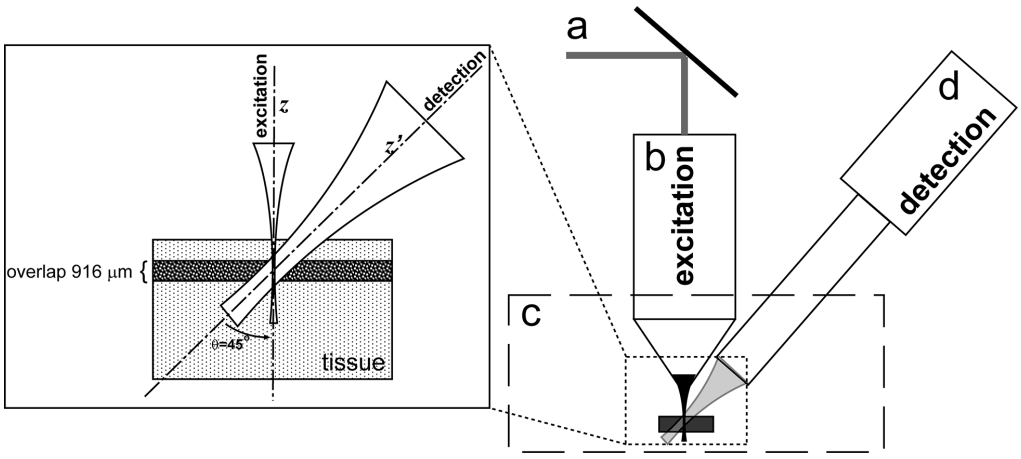

Figure 4. Schematic diagram of the off-axis PAM system. A) Excitation illumination, 355nm; B) 0.3 NA, water immersion optical objective; C) Water tank with sample; D) Focused ultrasonic transducer. Inset shows the focal overlap of the excitation and detection.

While resolution is negatively affected by off-axis detection, the ability to measure weak signals at depth is enhanced. Off-axis detection has an inherent dark-field quality; chromophores excited outside the numerical aperture of the ultrasonic detector will not be detected. Strong signals generated at shallow depths will not mask weaker signals deep in the tissue.

The area in the tissue where signal may be generated and detected is the region of overlap of the laser excitation and the focused detection, labeled in the inset of Figure 4. The overlap region of the transducer along the optical axis is the projection of the transducer beam waist onto the optical axis. The beam waist of a focused transducer can be approximated using an approach analogous to Gaussian optics approximations for determining beam waist, in which the ratio of focal length to source diameter dictates the beam waist resulting from the focusing lens [41]. The projection of the detection waist at the focus is then

$$Overlap = \frac{1.02Fv}{fD \sin\theta} \quad (3)$$

where F is the focal length of the acoustic optics, f is the transducer center frequency and D is the transducer element diameter. In order to maintain lateral resolution, the overlap region should not exceed the depth of focus of the laser excitation. Within this constraint, overlap may be maximized to improve cross-sectional imaging speed or reduced for improved sensitivity by reducing or increasing the detector numerical aperture, respectively.

It should be noted that Equations 2 and 3 are related by the transducer center frequency. Increasing the bandwidth (BW) will nominally increase the center frequency (f). We cannot arbitrarily increase the bandwidth to improve axial resolution while maintaining the same overlap without compensating by modifying the transducer focal length and/or element diameter. A reasonable compromise between imaging speed and sensitivity would be a transducer that yielded an overlap of 5 times the axial resolution; hence, 5 axial pixels would be acquired per A-line. In order to maintain this relationship, the ratio of F/D would need to be ~ 4.5, a ratio that is readily achieved even in standard high frequency commercial transducers.

As illustrated by the dark horizontal band in the inset of Figure 4, a B-scan recorded with off-axis PAM has an axial dimension (or size) defined by the overlap of the laser excitation and the ultrasonic detection. Consequently, if the overlap region is smaller than the depth to be imaged, B-scans at various depths would need to be acquired in order to build-up a full cross-sectional image. The number of B-scans

required for one cross-sectional image is a function of the desired imaging depth and the excitation/detection overlap.

The angle between the excitation objective and ultrasonic transducer was set to 45º±3º using a protractor. The angle was verified by measuring the signal from a human hair at two known axial positions and calculating the angle based upon Equation 1. The axial resolution and overlap were calculated to be 424 μm and 916 μm, respectively, based upon a 45º angle and the transducer specifications.

Results and discussion

The FWHM of the hair in the lateral dimension of the PAM image (Figure 5a) was 70 μm, in good agreement with the light microscope measurement. The FWHM of the hair in the axial dimension was 410 μm, estimated by measuring the FWHM of the envelope of the photoacoustic signal collected from a single A-line. Given the known diameter of the hair (65 μm), the measured axial FWHM should be a reasonable approximation of the axial resolution. The measured FWHM in both dimensions are consistent with the expected lateral (26 μm) and axial (424 μm) resolutions. The axial resolution can readily be improved by utilizing higher frequency transducers. Using a 50 MHz center frequency transducer (V358-SU, Olympus NDT) with an 80% bandwidth and nominal element size of 0.25 inches would provide an axial resolution of 53 μm in the current system. Similarly, using a 100 MHz transducer as in [29] and [40] would yield an axial resolution of 21 μm.

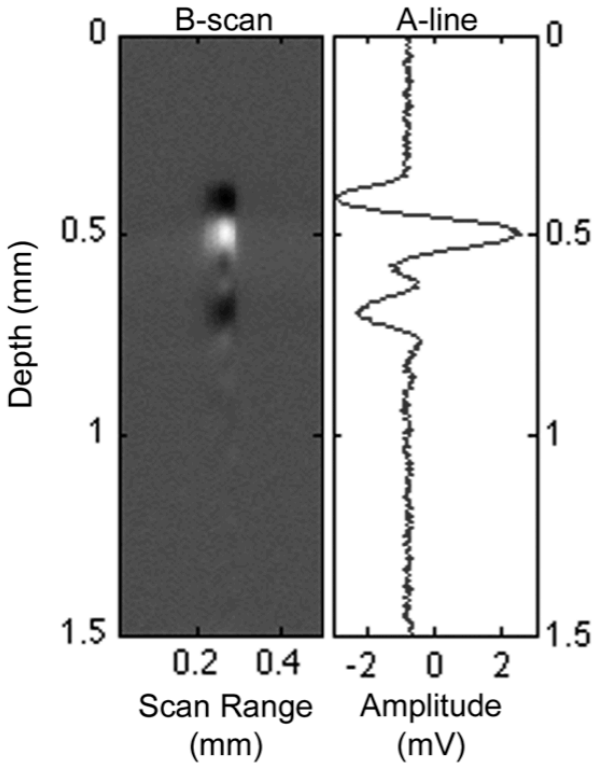

Figure 5. A demonstration OA-PAM imaging a human hair. A) B-scan image of a 65 µm human hair embedded ~500 µm in chicken breast tissue. B) A-scan corresponding to the center of the hair sample indicated by the arrow in A.

As higher frequency transducers are investigated, acoustic attenuation will become an important issue. The acoustic attenuation in water (and presumably water based acoustic coupling gel) is ~0.15 dB/mm at 25 MHz and ~2 dB/mm at 100 MHz [40]. The physical geometry of Off-Axis PAM enables the placement of the ultrasonic transducer at the minimum distance from the sample, with no obstructions between the sample and transducer. This may prove to be an additional advantage of off-axis PAM over designs that incorporate long working distance ultrasonic transducers and/or require the propagation of the acoustic wave through the laser excitation optics to achieve co-axial detection.

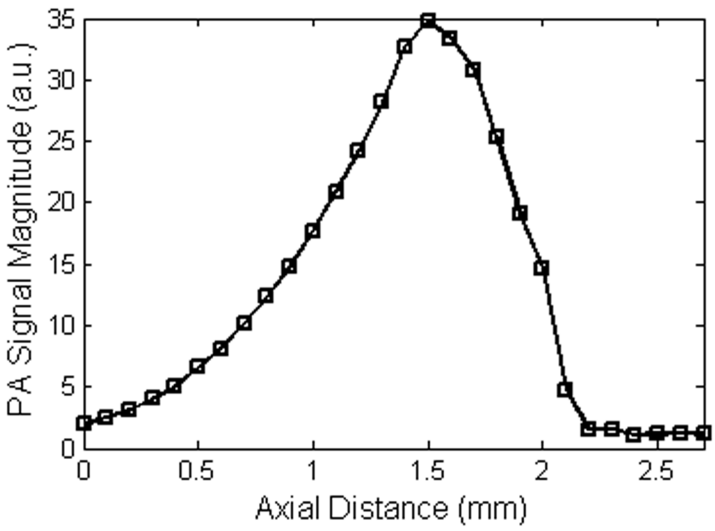

Figure 6. Map of the excitation/detection overlap. Maximum signal intensity was measured as a function of axial distance. The FWHM of the overlap was 900 μm.

A series of measurements have been made to map out the excitation/detection overlap region and to illustrate the quasi dark-field property inherent to off-axis PAM. A black human hair (diameter ~ 100 μm) submerged in water was translated in the axial dimension through the focus of the ultrasonic transducer. Photoacoustic B-scans were recorded at 100 μm axial increments. Each point in Figure 6 represents the maximum amplitude in each B-scan plotted against the axial position. Since the hair diameter was approximately an order of magnitude smaller than the theoretical overlap and the depth of focus of the excitation was 3 mm, the line shape in Figure 6 is expected to be a good approximation to the excitation/detection overlap. The FWHM of the measured overlap was ~ 900 μm, which was in good agreement with the theoretical overlap of 916 μm

derived from Equation 3. These results verify the quasi dark-field property of off-axis PAM.

In the design of an off-axis PAM system, the overlap region may be tuned by changing the numerical aperture and/or changing the center frequency of the ultrasonic transducer. For instance, using a 25 MHz center frequency transducer with a similar numerical aperture would yield an overlap of 219 μm in the current system. For the fastest imaging speed, a large overlap would be desirable in order to maximize the depth region probed in a single B-scan. For high sensitivity, the overlap region should be reduced in order to strongly attenuate photoacoustic signals away from the center of the overlap.

The maximum permissible exposure for skin set by the American National Standards Institute in the ultraviolet range is 3.5 mJ/cm^2. The 355 nm pulses used in this experiment resulted in a surface fluence of 0.99 mJ/cm^2, which approaches, but does not exceed, the permissible limit. Signal averaging could be done in order to lower the fluence of the excitation illumination on the tissue without lowering the signal to noise ratio. Additionally, if the excitation wavelength was moved to 532 nm, less pulse energy would be required to deposit the same amount of energy into the absorber at a given depth due to the strong $1/\lambda^4$ wavelength dependence of scattering.

Conclusions

In conclusion, a novel photoacoustic microscope design has been developed, which substantially simplifies construction by enabling the use of unmodified

commercial optics and ultrasonic transducers. Moreover, the simple design may be readily incorporated into a standard light microscope, thus providing a familiar imaging platform for clinical researchers. Appropriate equations have been derived to describe the relevant design parameters and the equations were verified via measurements made on the prototype OA-PAM system. A consequence of the simple design is a reduction in axial resolution compared to coaxial designs. The reduction is inversely proportional to the cosine of the angle between excitation and detection and equal to 15% and 41% for angles of 30º and 45º, respectively. In addition to design simplicity, the off-axis geometry may provide enhanced sensitivity from quasi dark-field detection and a reduced sample-to-transducer distance that will help mitigate the problem of high acoustic attenuation inherent to high-resolution, high-frequency transducers.

Analysis of post processing algorithms for photoacoustic microscopy

This section of Chapter II analyzes two proposed methods for processing PAM signals to achieve a better representation of the morphology of the spatial signal distribution. Relevant theory is discussed and direct comparisons are made on *ex vivo* vasculature samples.

Introduction

Within the last decade, photoacoustic microscopy (PAM) has established itself as a high-resolution, hybrid imaging technique with excellent sensitivity to optical absorption [29, 40, 42]. PAM combines the fine spatial resolution and high absorption

contrast of optical imaging with the high sensitivity and improved penetration depth of ultrasound imaging to produce high resolution, background-free images of blood, melanin, and other biological chromophores. Mapping of microvasculature [43], functional imaging of oxygen saturation and hemoglobin tracking [27], and detection of melanoma cells [44] are a few applications for which PAM has been used in the past few years.

Cellular and sub-cellular transverse resolution in PAM came with the advent of optical resolution PAM (OR-PAM), where the optical excitation beam waist governs the transverse resolution [29] of the microscope. Fully resolved capillaries [45], red blood cells [46], and cell nuclei [25] have been imaged using this technique. Others have built upon the OR-PAM model by laser scanning inside the focus of the transducer [47], improving the speed and footprint of PAM systems by introducing fiber and microchip lasers [48], and using adaptive optics to partially overcome the scattering effects that plague all high resolution optical imaging systems, improving the resolution of OR-PAM in highly scattering media [49].

Off-axis photoacoustic microscopy (OA-PAM) [50] is an adaptation of optical resolution PAM previously described in this chapter. In OA-PAM, the illumination and detection axes are separated in order to simplify the implementation of the photoacoustic microscope. Separating these axes negates the requirement for custom optics and transducers typically used in co-axial illumination/detection schemes, allowing off-the-shelf, commercial components to be used for the illumination objective and detection

transducer. As a result, higher beam quality and simplified design geometries are possible in exchange for a modest decrease in axial resolution.

Although the transverse resolution of OR-PAM based techniques is determined by the optics, the axial resolution is still derived from the time-of-flight acoustic signals recorded by the ultrasound transducer. Defined as the material sound velocity divided by the -6 dB transducer bandwidth, the axial resolution is on the order of 10s to 100s of microns for most transducers. A typical photoacoustic signal has a bipolar (N-shaped) pressure profile, which is converted to a bipolar voltage signal by the transducer. Consequently, photoacoustic A-lines (1-D depth profiles) and B-scans (2-D depth cross-sections) exhibit positive and negative peaks, which do not accurately represent the morphology of the photoacoustic signal source.

Bipolar signals can be found in many imaging arenas. Both ultrasound imaging and magnetic resonance imaging (MRI) collect bipolar signals and use them to produce morphologic images [51]. These techniques use the concepts of demodulation and signal enveloping to process the time oscillating signals into meaningful images. Demodulation and signal enveloping have long been used in the field of ultrasound imaging and MRI, but have not often been applied to photoacoustic imaging. While some backprojection reconstruction algorithms used in photoacoustic tomography (PAT) and thermoacoustic computed tomography (TCT) employ Weiner [52] and impulse [53] deconvolution, PAM images are almost exclusively published raw or as maximum amplitude projection (MAP) images. MAP images produce an accurate representation of the distribution of

features in the transverse dimensions of the volume, but they discard most of the available depth information.

In this study, two potential processing techniques for PAM are compared and evaluated. The proposed techniques are quadrature demodulation and Hilbert transform enveloping. The quadrature demodulation technique is often used in lock-in detection, in which a periodic signal of interest is frequency-mixed with a reference signal of the same frequency, resulting in a sum-frequency component at 2ω and a difference-frequency component at baseband. A low pass filter is then used to extract the original signal, which has been demodulated and is now relatively free of frequency-dependent noise. The Hilbert transform enveloping technique consists of using the collected data to build an analytic signal, which is a combination of the original signal and its Hilbert transform. The magnitude of this complex signal is then computed to extract the envelope of the time domain signal. Both of these methods are used for post processing in ultrasound imaging [51, 54], so photoacoustic microscopy is a natural extension of their application.

In order to better illustrate these techniques, consider a signal $s(t) = V_S \sin(\omega t + \phi_S)$, which will represent the center frequency component of a photoacoustic A-line. In reality, the A-line is a broadband signal composed of many sine waves, but a single frequency will be used for the purpose of illustration. Multiplying this signal with a reference signal of equal frequency, $s_R(t) = V_R \sin(\omega t + \phi_R)$, yields

$$
\begin{aligned}
s_M(t) &= s(t) \times s_R(t) \\
&= V_S V_R \sin(\omega t + \phi_S) \sin(\omega t + \phi_R) \\
&= \frac{1}{2} V_S V_R \cos(\phi_R - \phi_S) + \frac{1}{2} V_S V_R \sin(2\omega t + \phi_R + \phi_S)
\end{aligned} \tag{4}
$$

where $s_M(t)$ is the resulting signal from the mixing of the signal of interest and the reference signal, V_S and V_R are the signal amplitudes of the photoacoustic signal and the reference signal, respectively, ω is the signal frequency, and ϕ is the signal phase. Equation 4 shows the frequency components at DC and 2ω that arise from the mixing of the photoacoustic signal with the reference signal. As can be seen in Equation 4, the phase of both the photoacoustic signal and the reference signal must be known in order to extract an accurate value of V_S. While the reference signal phase can easily be monitored, the phase of the collected signal is generally unknown. This dependence on the signal phase can be mitigated, however, by computing an additional mixed signal using a reference signal with a ninety-degree phase shift. The new reference signals that will be used are in quadrature and defined as follows:

$$
\begin{aligned}
s_{R1}(t) &= V_R \sin(\omega t + \phi_R) \\
s_{R2}(t) &= V_R \sin\left(\omega t + \phi_R - \frac{\pi}{2}\right)
\end{aligned} \tag{5}
$$

Taking the product of the reference signals in Equation 5 and the original signal, $s(t)$, yields the following mixed signals:

$$s_{M1}(t) = \frac{1}{2}V_S V_R \cos(\phi_R - \phi_S) + \frac{1}{2}V_S V_R \sin(2\omega t + \phi_R + \phi_S)$$
$$s_{M2}(t) = \frac{1}{2}V_S V_R \cos\left(\phi_R - \phi_S - \frac{\pi}{2}\right) + \frac{1}{2}V_S V_R \sin\left(2\omega t + \phi_R + \phi_S - \frac{\pi}{2}\right) \quad (6)$$

It is necessary to use two reference signals to reconcile unknown phase differences between the original signal and the reference signal. These mixed signals, representing the in-phase and out-of-phase components of the signal, are then lowpass filtered around the baseband signal component. The bandwidth and cutoff frequency of the filter are determined by the frequency content of the resulting photoacoustic signals. This is generally governed by the bandwidth and center frequency of the transducer, but is affected by several other parameters as well. The magnitude of the resulting filtered signals is then taken by computing the square root of the sum of squares, effectively yielding a phase-independent envelope of the photoacoustic A-line:

$$s_{MAG} = \sqrt{{s_{M1}}^2 + {s_{M2}}^2} \quad (7)$$

In addition to quadrature demodulation, a Hilbert transform enveloping technique used in ultrasound imaging [54] was also investigated for the processing of the photoacoustic A-lines. While the Hilbert transform technique is not nearly as popular as quadrature demodulation, it has some distinct benefits and is worthy of consideration. The Hilbert transform is essentially a sign-dependent phase shifter. The Hilbert transform of a signal $s(t)$ can be described mathematically as the convolution of a signal with a shaping function, i.e.

$$\hat{s}(t) = \frac{1}{\pi t} * s(t) \tag{8}$$

where $\hat{s}(t)$ is the Hilbert transform of the signal. Practically, the Hilbert transform is performed by taking a Fourier transform of the signal, then phase shifting the signal by multiplying the positive frequencies of the Fourier spectrum by $-j$ and the negative frequencies by j. The inverse Fourier transform is then taken to complete the Hilbert transform. In order to obtain the signal envelope using the Hilbert transform, an analytic signal is constructed by taking a signal and adding its Hilbert transform in quadrature, i.e.

$$s'(t) = s(t) + jH\{s(t)\} \tag{9}$$

where $s'(t)$ is the analytic signal and $H\{\cdot\}$ is the Hilbert transform operator. The envelope of the original signal $s(t)$ can then be extracted by computing the magnitude of $s'(t)$ through the square root of the sum of squares, i.e.

$$g(t) = \sqrt{s(t)^2 + jH\{s(t)\}^2} \tag{10}$$

where $g(t)$ is the envelope of the A-line, $s(t)$.

In order to better illustrate how these processing techniques are implemented on a typical photoacoustic A-line, the techniques were applied to the factory-shipped time-domain transducer response of a focused 6 MHz ultrasound transducer (V305-SU, Olympus NDT). The response was obtained by recording the echo from a steel ball submerged in water. Figure 7 contains four panels illustrating the demodulation techniques described above. Panel A shows the time-domain transducer response

measured by Olympus, Inc., which corresponds to $s(t)$ in the above equations. Panel B shows the mixed time domain signals, i.e. the results of Equation 6. Panel C shows the frequency content of panel B, with significant frequency components at baseband and 12 MHz, as well as the frequency content of the transducer response (panel A), shown by the dashed line. Panel D shows the original transducer response (raw A-line), the A-line processed using quadrature demodulation (result of Equation 7), and the A-line processed using the Hilbert transform envelope technique (result of Equation 10).

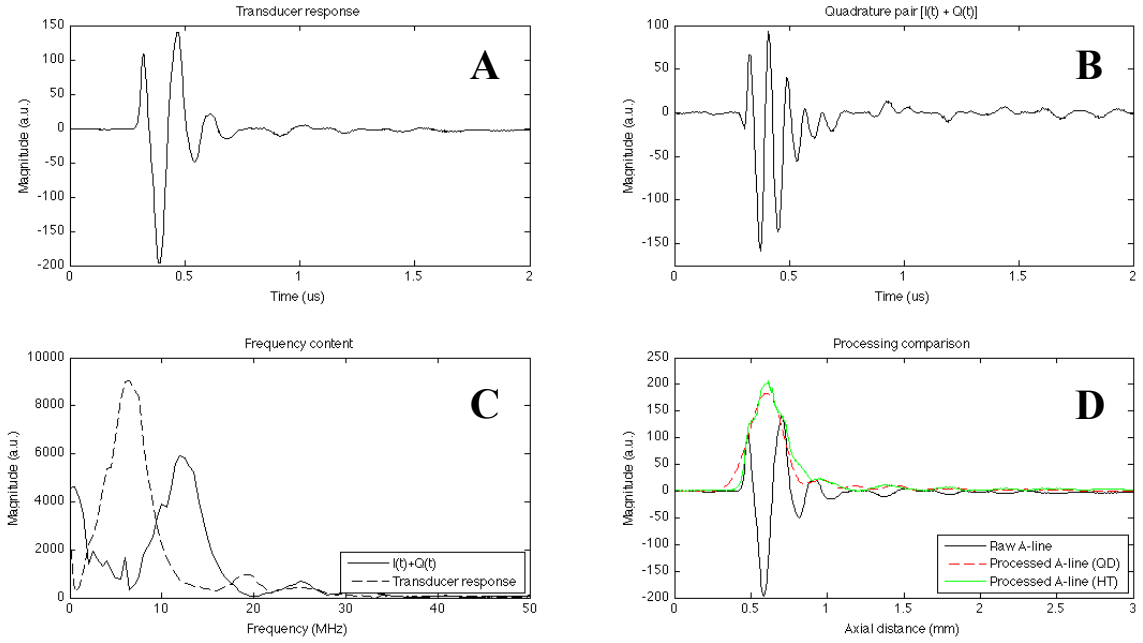

Figure 7. Illustration of demodulation techniques on the factory response of a 6 MHz ultrasound transducer. Panel A shows the time domain transducer response. Panel B shows the mixed time domain quadrature pair signals. Panel C shows the frequency content of panels A and B, illustrating the movement of the frequency content to 2ω and baseband. Panel D shows the transducer response with the processed responses overlaid. Note that the envelope obtained through the quadrature demodulation technique was multiplied by a factor of two for ease of comparison.

Both of the processing techniques result in accurate representations of the envelope of the time domain transducer response. Each method gives a FWHM linewidth of ~ 270 μm, which is reasonable given the theoretical axial resolution of 285 μm calculated from the transducer bandwidth and the speed of sound in water. However, there is a distinct difference in the shape of the envelope when the A-line is processed using these methods. The quadrature demodulation gives a very smooth profile with no ripple in the signal envelope, while the Hilbert transform method yields an envelope with minor ripples throughout the signal peak. Generally speaking, this ripple is undesirable for imaging, as it distorts what should be expected to be a homogenous signal source.

One notable advantage of the Hilbert transform technique, however, is the lack of need for any *a priori* information regarding the frequency content of the A-line. In order to optimize the accuracy of the quadrature demodulation, the reference signal frequency should be matched to the centroid of the collected frequency spectrum. However, the peak frequency of the collected photoacoustic signal does not always match the peak frequency of the transducer. There are other factors, such as the dimensions of the absorption volume, structure of the absorbing specimen, and the pulse width of the excitation light that also affect the shape of the spectral content. For this reason, it is not always reasonable to assume the peak signal frequency is equal to the peak transducer frequency. Ideally, the centroid of the spectral content of the A-line would be ascertained before an accurate quadrature demodulation could be performed on a given A-line. An additional advantage of the Hilbert transform technique is that the magnitude of the full

signal bandwidth is extracted, while quadrature demodulation throws away half of the signal content when the demodulation occurs. As a result, the magnitude of the envelope using the Hilbert transform technique is twice that of the envelope using quadrature demodulation.

Another consideration when comparing these techniques is processing overhead and implementation. Quadrature demodulation has a relatively low processing overhead, since all of the signal manipulation can be done in the time domain. Furthermore, quadrature demodulation can be implemented almost entirely in hardware, using RF mixers and filters. This presents a significant speed advantage. The Hilbert transform envelope technique, however, requires two Fourier transforms, which adds considerably to the processing overhead. For this reason, Hilbert transform approximations [55] are typically used in real-time, high frame rate imaging instead of the true transform. Fortunately, this processing overhead is acceptable for most standard imaging applications of PAM. The Hilbert transform technique also provides access to the complex phase information of the A-line, if such information is desired.

Methods and materials

A modified OA-PAM system was built for these experiments, expanding upon the original off-axis design, which can be found in [50]. The excitation source of the modified system was a Q-switched, DPSS laser (1Q 532-2, Crylas) frequency doubled to 532 nm with pulse duration of 1.3 ns and a 10 kHz maximum repetition rate. 532 nm is an excellent wavelength for imaging vasculature while retaining an acceptable

penetration depth. The beam was passed through an underfilled 0.3 NA water immersion objective with a long working distance, resulting in a theoretical transverse resolution of ~ 3.3 μm. The photoacoustic signals were collected using a 25 MHz, focused ultrasonic transducer (V322-SU, Olympus NDT) with a -6 dB bandwidth of 55%, an element size of 6 mm and an effective numerical aperture of 0.16. The photoacoustic signals were then amplified using a broadband radio frequency amplifier (ZFL-500LN, Mini-Circuits) and digitized with an oscilloscope (DPO-7254, Tektronix). The oscilloscope was triggered by a photodiode measuring a small portion of each laser pulse. Image scanning was accomplished using an automated micro-stepping stage (M-562, Newport Corp) to translate the sample.

The consequences of off-axis detection have been described in detail in the previous section. There is a reduction in axial resolution equal to the reciprocal of the cosine of the detection angle. This reduction is illustrated in Equation 3. For the work done in this study, a detection angle of 45 degrees was used, which results in a 41% reduction in axial resolution. Using Equation 3, this results in a theoretical axial resolution of ~155 μm for the transducer used in these experiments.

Results and discussion

In order to evaluate the imaging capabilities of the improved OA-PAM system and effectiveness of each algorithm, an acceptable biological sample for volumetric imaging was chosen. The cheek pouch of a Syrian hamster is a common animal model for oral cancer and the cheek pouch has a rich microvasculature, which made it an

excellent choice. The cheek pouches were excised from freshly sacrificed hamsters and placed in the imaging system. The thickness of the cheek pouch was ~ 500 μm. Vessel size ranged from capillaries (~ 10 μm diameter) to larger vessels (~200 μm diameter). Large vessels were cauterized before being placed in the water bath to prevent excessive blood loss in the vessels of interest. The data was taken as volumetric raster scans at a laser repetition rate of 400 Hz. One pulse of 80 nJ was used per spatial point. Volumetric stacks of 1000x100x1000 pixels were acquired at a spatial sampling of 1 μm along the fast axis and 10 μm along the slow axis in the transverse dimensions. A MAP image was obtained from the volume stack to verify the imaging capabilities of the photoacoustic microscope. For this image the dimension along the fast axis was spatially averaged with a 10-pixel window. Figure 8 shows a 1 mm^2 MAP image of the vasculature in the cheek pouch. Very small vessels, assumed to be capillaries, as well as much larger vessels can be seen in the image. A bifurcation of the largest vessel in the image is also evident.

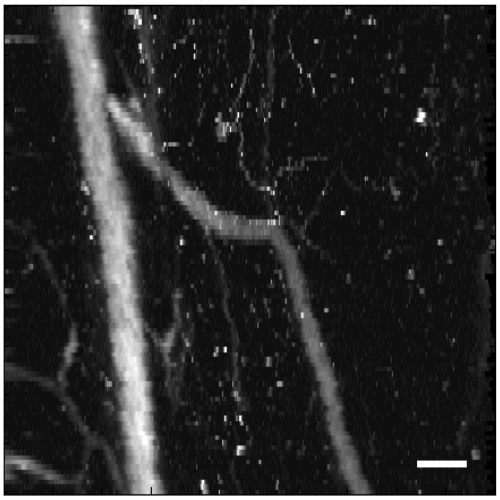

Figure 8. Maximum amplitude projection (MAP) image of vessel network in the excised cheek pouch of a Syrian hamster. Scale bar = 100 microns.

Upon observing favorable results from the post processing of the theoretical A-line and verifying the imaging capabilities of the OA-PAM system, the algorithms were applied to the experimental data obtained from the cheek pouches. Figure 9a shows a comparison of a raw A-line (left) with A-lines processed using quadrature demodulation (center) and Hilbert envelope filtering (right). Both processing techniques succeed in approximating the envelope of the time domain A-line signal; however, as previously observed, the quadrature demodulation results in a smoother envelope. Figure 9b illustrates the improved contrast and morphologic accuracy of the filtered techniques in B-scan images (center and right) when compared to a raw B-scan image (left). The B-scans depict cross-sections of blood vessels in the cheek pouch.

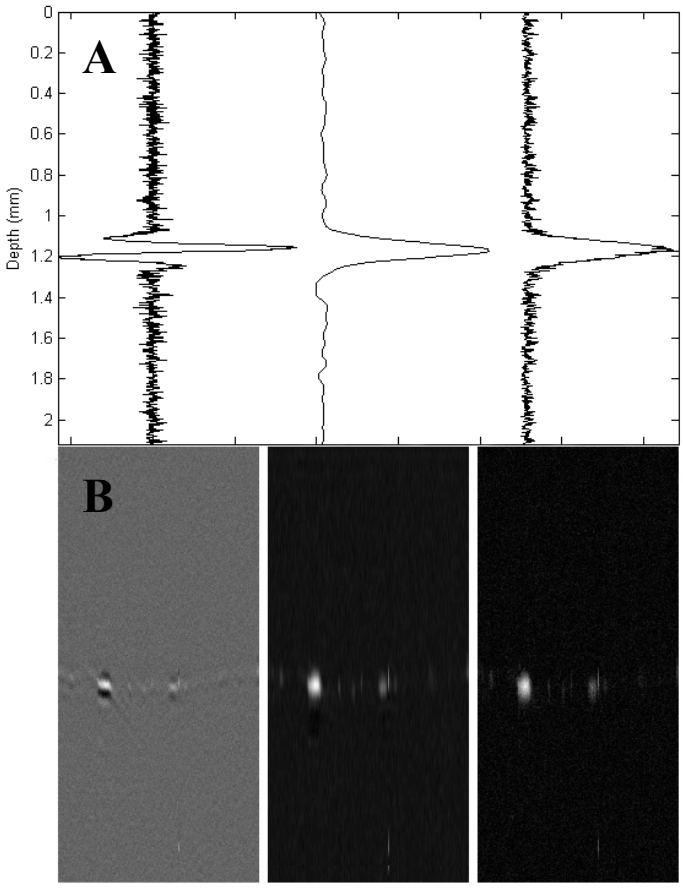

Figure 9. Processing comparison on *ex vivo* hamster vasculature. (A) A-lines through a blood vessel in the cheek pouch of a Syrian hamster: unprocessed (left), processed using the quadrature demodulation technique (middle), and processed using the Hilbert transform envelope technique (right). (B) B-scans of blood vessels showing unprocessed (left), processed using the quadrature demodulation technique (middle), and processed using the Hilbert transform envelope technique (right). Scale bar = 200 microns.

It is important to note the morphology represented in the raw image when compared to the processed images. Due to the sinusoidal nature of the raw photoacoustic A-line, the raw B-scan image of the blood vessel has high and low intensity stripes. This is a poor representation of the signal source, which is expected to be relatively uniform.

The sinusoidal nature of the signal also makes it very difficult to estimate the vessel size in the axial dimension. When the raw signal is properly processed, the axial dimension of the image shows a structure that is consistent with the vessel size (in the case where the axial resolution is sufficient to properly resolve the vessel) or the axial resolution (in the case where the vessel is much smaller than the axial resolution). In this case, the vessels are smaller than the axial resolution of the transducer, so the vessel diameter in the axial dimension is approximated by the axial resolution.

As discussed previously, both quadrature demodulation and the Hilbert transform envelope method have distinct merits depending on the application requirements. In these experiments, the processing was done after the data was acquired, so processing overhead was not a significant concern. Moreover, the peak signal frequency was not guaranteed to be constant over the imaging volume, so the Hilbert transform envelope was deemed to be most suitable. Figure 10 shows a 1 mm^3 volumetric reconstruction of the vasculature in the hamster cheek pouch taken from the same dataset that produced the MAP image above, processed using the Hilbert transform envelope method.

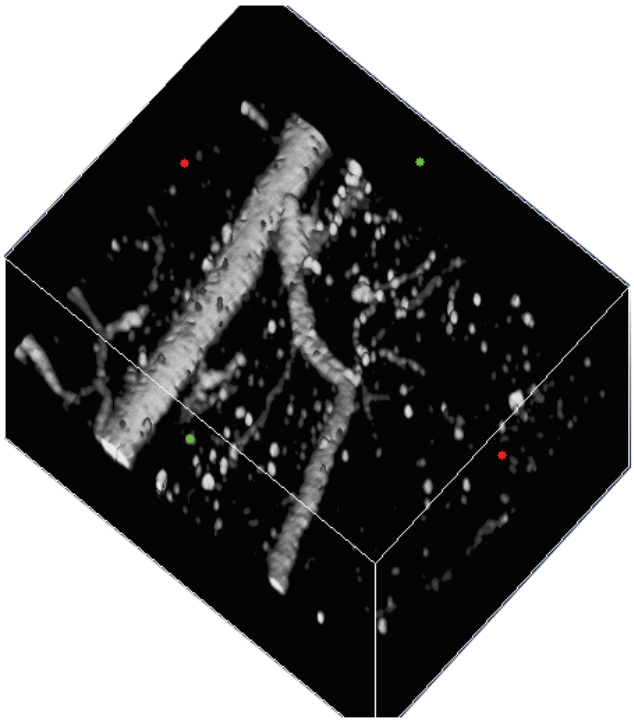

Figure 10. Volumetric reconstruction of vessel network in the excised cheek pouch of a Syrian hamster. Volume stack was post processed using the Hilbert transform enveloping technique.

Conclusion

Off-axis photoacoustic microscopy was used to acquire volumetric datasets of microvasculature in the cheek pouch of a Syrian hamster. Quadrature demodulation and Hilbert transform enveloping were investigated and evaluated as methods for A-line processing. Both processing methods produce higher contrast A-lines that provide a better representation of the axial point spread function of the imaging system when compared to unprocessed a-lines. Advantages of quadrature demodulation include reduced processing overhead, a smoother envelope, and the ability for the algorithm to

be implemented in hardware. Advantages of the Hilbert transform enveloping technique include the ability to accurately process the A-line without *a priori* information regarding the spectral content, a two-fold increase in envelope magnitude, and access to the signal's complex phase information. Regardless of which method is used, envelope processing of the raw data leads to overall improvement of image quality and interpretation.

CHAPTER III

TRANSIENT ABSORPTION ULTRASONIC MICROSCOPY*

Initial prototype and theory

This section of the manuscript introduces the concept of combining photoacoustic microscopy with transient absorption (pump-probe spectroscopy) and details the relevant theory, methods, and results.

Introduction

Photoacoustic microscopy (PAM) is a recently developed high-resolution, absorption-contrast imaging modality primarily applied to imaging in turbid media, such as tissue. Typical chromophore targets include hemoglobin [25], melanin [24], gold nanoparticles [56], and dyes [57]. The weak attenuation of acoustic emission permits high-resolution imaging in tissue up to several millimeters deep [40]. Recent advances have significantly improved the lateral spatial resolution by optically limiting the excitation volume [29] enabling submicron lateral resolution [46]. While the lateral resolution is optically limited, the axial resolution is limited by the bandwidth of the ultrasonic detector, estimated to be ~15 μm (75 MHz detector) in [29], yielding a highly asymmetric voxel.

---

*Part of this chapter was reprinted with permission from "Ultrahigh resolution photoacoustic microscopy via transient absorption" by R. L. Shelton and B. E. Applegate, 2010. *Biomedical Optics Express*, 1, 676-686, Copyright 2010 by OSA.

Higher axial resolution and a more symmetric voxel would be advantageous for high-resolution imaging. The axial resolution is linearly dependent on the detector bandwidth. An axial resolution of 1.5 μm would require a 1 GHz bandwidth detector. Detecting such high acoustic frequencies poses several problems including detector construction, acoustic dispersion and acoustic attenuation. A 300 MHz acoustic wave is attenuated at a rate of ~20 dB/mm in water and ~80 dB/mm in tissue, which would practically limit the imaging depth to ~100 μm [29]. Simply increasing the detector bandwidth does not appear to be an effective approach to a more symmetric voxel.

This chapter will detail an alternate approach, Transient Absorption Ultrasonic Microscopy (TAUM), which uses optical nonlinearities to optically limit the spatial resolution in *both* the axial and lateral dimensions. The approach effectively fuses pump-probe absorption spectroscopy with photoacoustic microscopy. Pump-probe absorption spectroscopy is a well-established tool in molecular physics for measuring the spectrum and dynamics of molecular species that exhibit low fluorescence quantum yield. In fact, the relaxation dynamics of DNA after absorption of UV light has recently been studied using pump-probe absorption spectroscopy [58]. The specific pump-probe technique employed here is designed to measure a transient change in the ground state population of the target chromophore.

Pump-probe spectroscopy inherently measures pump-induced changes in the attenuation of the probe. On a molecular level, interaction with the pump radiation induces changes in molecular state populations. The probe interrogates these population changes and reports via a pump dependent change in the probe attenuation. If the pump

is amplitude modulated, the modulation will be transferred to the probe. Nominally, the probe must be delayed in time relative to the pump. If the probe signal is measured as a function of the interpulse pump-probe delay, the signal should map out an exponential that decays at a characteristic time corresponding to the time it takes the molecular state population to return to equilibrium. This time is often referred to as the ground state recovery time of the molecule.

The pulsed laser induced photoacoustic emission, $p(r,t)$, from a molecular absorber may be written as

$$p(r,t) = \sigma N_1 F \kappa(r,t) \tag{11}$$

where σ is the absorption coefficient, N_1 is the ground state population density, F is the laser fluence, and $\kappa(r,t)$ is a term describing the space and time-dependence of the pressure profile, as well as the material properties of the absorber. This equation is more traditionally expressed in terms of the absorption coefficient, μ_a, where $\mu_a = \sigma N_1$. As noted above, the pump will change the population, N_1, thereby changing the photoacoustic emission from the probe. In order to illustrate the underlying physics we will utilize a simple two-state system, for which we have previously derived the relevant equations governing the time dependent state populations [59, 60].

Consider a two-state molecular system isolated in an ideal solvent that quenches the excited state with a time constant τ resulting in photoacoustic emission. If the pump pulse duration is much less than τ and the transition is far from saturation, the population of the ground state after interacting with a pump pulse is given by

$$N_1 = N_1^0 \left[1 - \frac{\sigma \lambda_{pu} F_{pu}}{hc} exp\left(-\frac{t_d}{\tau}\right)\right] \quad (12)$$

where $N_1{}^0$ is the initial (before interacting with pump radiation) ground state population, λ_{pu} is the pump wavelength, F_{pu} is the pump fluence, h is Planck's constant, c is the speed of light, and t_d is the interpulse delay between the pump and probe. The pump-probe signal may be extracted by taking the difference in the photoacoustic emission amplitude with pump on and off, i.e.

$$\Delta p(r,t) = \sigma N_1^0 \left[\frac{\sigma \lambda_{pu} F_{pu}}{hc} exp\left(-\frac{t_d}{\tau}\right)\right] F_{pr} \kappa(r,t) \quad (13)$$

Note the quadratic dependence on fluence; a property shared with other two-photon microscopy techniques.

Equation 13 is dependent on two molecular-specific physical properties, σ and τ. The wavelength dependence of the absorption coefficient, σ, may be measured by recording the signal as a function of pump or probe wavelength. Similarly, the state recovery time, τ, may be measured by recording the signal as a function of interpulse delay (t_d) and fitting the result to an exponential decay. Both properties may be used to gain specificity for the target molecule.

The spatial resolution of TAUM is governed by the pump-probe interaction, rather than the ultrasonic transducer specifications. The point spread function resulting from the overlap of a pump and probe has been derived previously by Dong, et al. [61],

$$\mathrm{PSF}_{TAUM} = I(r,z) I'(r',z') \quad (14)$$

where the prime indicates the pump beam, the molecular transition is assumed to be far from saturation, and the light intensity profile is defined as

$$\mathrm{I}(r,z) = \left| 2\int_0^1 J_0(kr\sin\alpha,\rho) exp\left[\frac{1}{2} i4kz\sin^2\left(\frac{\alpha}{2}\right)\rho^2\right] d\rho \right|^2 \quad (15)$$

where r and z are the radial and axial coordinates, respectively, k is the wavenumber, ρ is the radial dimension in the polar coordinate system, and $\sin\alpha$ is the numerical aperture of the objective lens. If the pump and probe beams share the same wavelength, then Equation 14 simplifies to $PSF_{TAUM} = I(r,z)^2$, which is equivalent to the PSF for confocal microscopy and two-photon fluorescence microscopy [62]. TAUM should therefore be capable of subcellular, photoacoustic imaging in three dimensions. Just as in two-photon fluorescence microscopy, as the transition approaches saturation the resolution is degraded. If the transition is saturated along the entire depth of focus, there will be no sectioning from the pump-probe overlap.

A significant advantage of this pump-probe technique is that it is freed of any frequency restraints imposed on the transducer by axial resolution requirements. Transducers with center frequencies of 50 – 100 MHz are commonly used in photoacoustic microscopy to optimize the resolution in the axial direction. The downside to increasing the transducer frequency is that higher frequency acoustic waves are much more attenuated in tissue than lower frequency waves, resulting in much lower effective imaging depths for high frequency transducers. A 5 MHz acoustic wave is attenuated 200 times less in tissue than a 100 MHz acoustic wave [30]. In order to get an axial resolution of 1.5 μm (the theoretical optical resolution in the experiments described below), a 1 GHz transducer must be used. At these high frequencies, the attenuation of the acoustic waves in tissue is ~20,000 times greater. Since the resolution

in TAUM does not rely on the detector bandwidth, 1 μm resolution may be achieved even with low frequency ultrasonic transducers.

Methods and materials

A prototype TAUM system has been built in order to evaluate the potential of TAUM for high-resolution imaging. A schematic diagram of the system is shown in Figure 11. The excitation source was a Q-switched, 1064 nm, DPSS laser (1Q 532-2, Crylas), frequency doubled to 532 nm with pulse duration of 1.3 ns and a maximum repetition rate of 10 kHz. The output of the laser was directed to a beam splitter, where the forward propagated light formed the probe and the reflected light formed the pump. The pump and probe passed through either side of a dual frequency optical chopper before being recombined with a second beam splitter after the probe had been delayed ~ 1 ns relative to the pump. The ground state recovery time for hemoglobin at a wavelength of 532 nm is ~9 ns [59]. A delay of 1 ns was chosen as a value that was geometrically convenient for our system's implementation of the dual frequency chopper, but short enough to ensure sufficient population in the excited state when the probe is incident on the sample. The pump-probe signal is linearly dependant on the population of the probed energy state, therefore the pump-probe delay time is very important for optimal signal-to-noise. The recombined beam passed through a beam expander formed by L1 and L2. The beam was then focused onto the sample through one of two water immersion microscope objectives (NIR APO 40X/.80 3.5 mm WD, CFI W Plan Fluor 10X/.30 3.5 mm WD, Nikon), depending on the experiment. The

photoacoustic signals were collected using one of two focused ultrasonic transducers (V310-SU, V322-SU, Olympus NDT), depending on the experiment. The V310 is a 6 MHz center frequency transducer with a 6 mm element size, 80% (-6 dB) bandwidth, and a numerical aperture of 0.23. The V322 is a 25 MHz center frequency transducer with a 6 mm element size, 60% (-6 dB) bandwidth, and a numerical aperture of 0.16. For each experiment, the ultrasonic transducer was fixed at a 45º angle to the optical axis. The resulting photoacoustic signals from the transducer were then amplified through two radio frequency amplifiers (ZFL-500LN, Mini-Circuits), providing ~ 26 dB total amplification. The amplified signal was collected and digitized with a high-speed digital oscilloscope (DPO-7254, Tektronix), then processed and stored using a custom Labview GUI.

The 6 MHz transducer was used for the preliminary studies because that is what was available at the time of the experiment. The 25 MHz transducer was later acquired and used for the subsequent experiments due to the increased bandwidth, leading to the collection of more harmonic side bands (described below). The center frequency of the transducer is of little consequence to the TAUM signal; however, the bandwidth, which is ultimately limited by the center frequency of the transducer, determines the number of harmonics collected. There is some advantage in matching the transducer center frequency and the laser repetition rate, since this would concentrate the signal power in fewer harmonics over the detectors bandwidth. However, this strategy is only practical for MHz repetition rate laser sources.

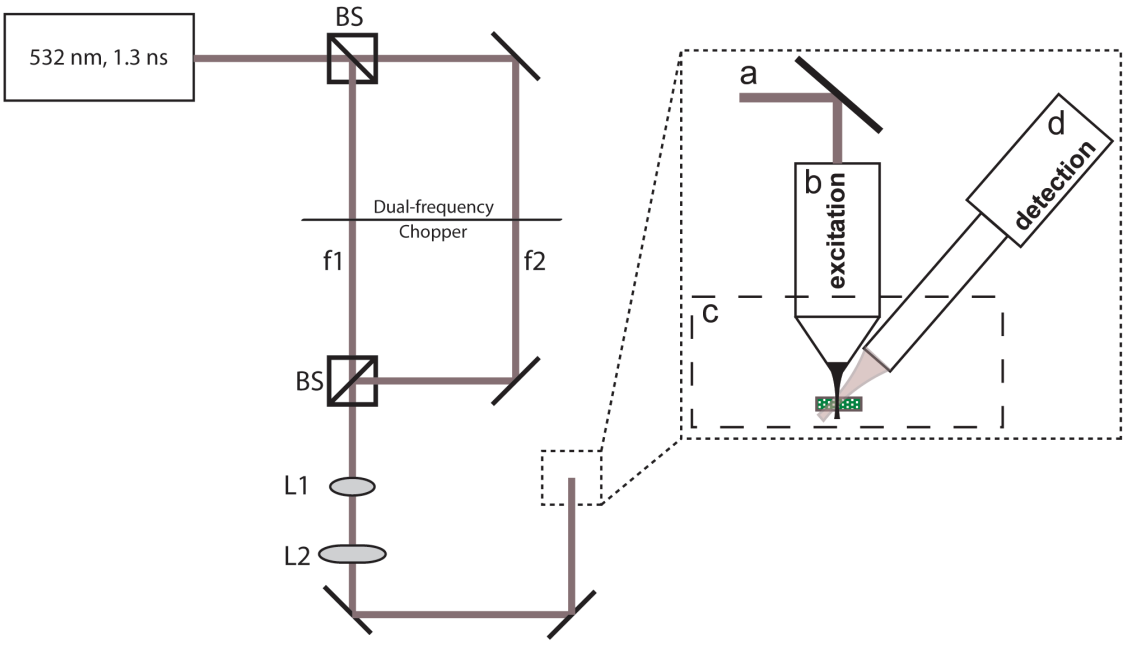

Figure 11. Schematic diagram of the prototype TAUM system. f1 and f2 are the modulation frequency of the pump and probe, respectively, as induced by a dual frequency optical chopper. L1 and L2 form a beam expander to fill the aperture of the objective (b). The sample is placed in a water bath (c) for acoustic coupling. A 6 or 25 MHz center frequency ultrasonic transducer serves as the detector (d).

While Equation 13 plainly illustrates the source of the pump-probe signal, simply calculating the difference in the temporal trace of the photoacoustic emission from an "on" and "off" experiment is prone to a number of noise and background sources more efficiently avoided in the frequency domain. For instance, the pump and probe photoacoustic signals are nearly completely overlapped in the time-domain making it impractical to detect pump-induced changes in the time-domain probe signal. However, since the pump and probe beams are modulated at different frequencies, they do not overlap in the frequency-domain. In order to implement frequency domain signal collection, the signal is frequency-encoded via amplitude modulation of the pump and

probe beams using a dual frequency optical chopper (3501, Newport Corp.) with a 42/30 ratio blade, capable of up to 4.48 kHz amplitude modulation. The transient absorption signal will then appear at the sum and difference frequencies of the pump and probe modulation, which may be readily extracted in the frequency domain.

The optical chopper imposes a square wave modulation on the pulse train of the laser. A square wave is well represented by a Fourier series containing only odd harmonics of the square wave frequency. Similarly, the pulsed source can be treated mathematically as a Fourier series, although all of the harmonics have a finite intensity. In both cases, the most intense band is the fundamental. Therefore, it is reasonable to derive the harmonic content of our signal by truncating the Fourier series after the first term. Moreover, by imposing a cosinusoidal modulation on the pump and probe fluence, the total time domain signal for the two-state system will be

$$p(r,t) = \sigma N_1^0 F_{pu}\left(\frac{1+\cos(\omega_{pu}t)}{2}\right)\left[1-exp\left(-\frac{t_d}{\tau}\right)\right]\kappa'^{(r,t)} + \sigma N_1^0\left[1-\frac{\sigma\lambda_{pu}F_{pu}\left(\frac{1+\cos(\omega_{pu}t)}{2}\right)}{hc}exp\left(-\frac{t_d}{\tau}\right)\right]F_{pr}\left(\frac{1+\cos(\omega_{pu}t)}{2}\right)\kappa(r,t) \quad (16)$$

where the first term is photoacoustic emission due to the pump and the second term is photoacoustic emission due to the probe. The pump (ω_{pu}) and probe (ω_{pr}) modulation frequencies are slow compared to the laser repetition rate. If we record $p(r,t)$ over a large number of laser pulses with an ideal pressure transducer at r_0 and Fourier transform into the frequency domain, then

$$P(r_0,\omega) = \mathrm{K}(r_0,\omega)\sum_{n=0}^{\infty}\Big[A\delta(n\omega_l) + B\delta\big(n\omega_l \pm \omega_{pu}\big) + C\delta\big(n\omega_l \pm \omega_{pr}\big) + D\delta\Big(n\omega_l \pm \big(\omega_{pu} \pm \omega_{pr}\big)\Big)\Big] \tag{17}$$

where ω_l is the laser repetition frequency, $\mathrm{K}(r,\omega)$ is the Fourier transform of $\kappa(r,t)$ which is notoriously broadband and resembles a log-normal distribution, the A, B, and C, coefficients are due to single photon photoacoustic emission and D is due to the pump-probe interaction, which for the two-state system described above is proportional to Equation 13 divided by $\kappa(r,t)$. Eight sidebands are associated with every harmonic (n) of the laser repetition frequency. A real pressure transducer will attenuate and bandpass $P(r_0,\omega)$, according to its spectral envelope. Thus, the TAUM signal is the piecewise integral of all of the D sidebands in the attenuated and bandpassed $P(r_0,\omega)$. A full derivation of Equation 17 can be found in Appendix A.

Figure 12 is a simulation of Equation 17 for n=1 assuming a 10 kHz laser repetition rate, a pump modulation of 1 kHz and a probe modulation of 0.7 kHz. Panel A is the signal with no modulation of the pump and probe. Panel B is the signal with the pump and probe modulated, but no pump-probe interaction. Panel C includes the bands due to the pump-probe interaction. The signals due to pump, probe, and the pump-probe interaction may be clearly delineated in the frequency domain.

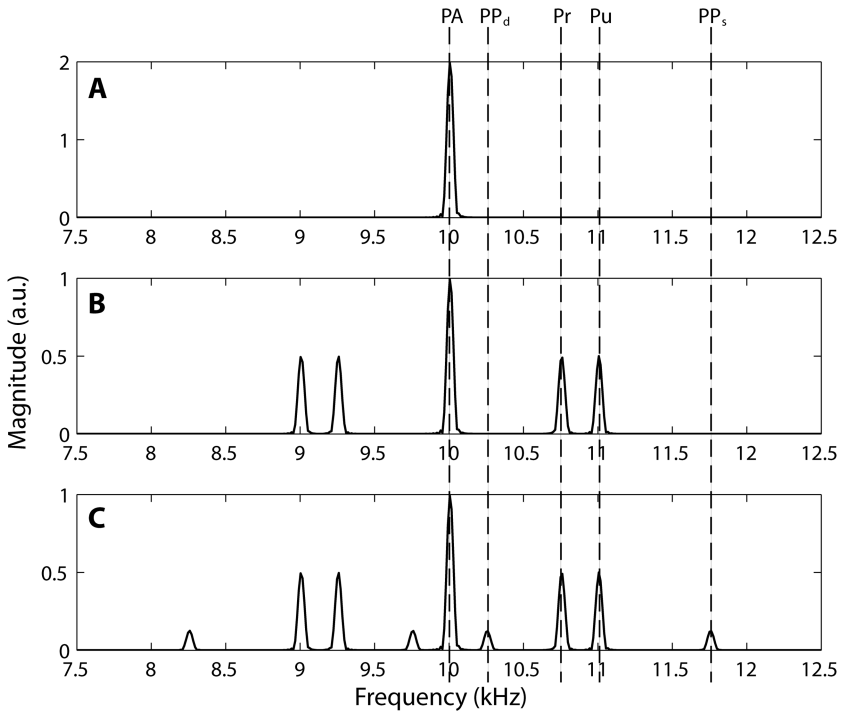

Figure 12. Simulation of $P(r_0,w)$ with n=1, Equation 17. Panel A shows the resulting frequency band due to single photon photoacoustic emission (PA) at the laser repetition rate of 10 kHz (w_l). Panel B includes the amplitude modulation of the pump (Pu) and probe (Pr) fluence, which adds beat frequencies of the pump and probe at 1 kHz ($\pm w_{pu}$) and 0.7 kHz ($\pm w_{pr}$), respectively to the 10 kHz band. All bands are due to single photon photoacoustic emission. Panel C includes the pump-probe interaction (coefficient D, Equation 17), which induces sidebands at the sum (PP_s), 1.7 kHz ($\pm(w_{pu}+ w_{pr})$) and difference (PP_d), 0.3 kHz ($\pm(w_{pu}- w_{pr})$) of the pump and probe modulation.

In practice, the time domain photoacoustic signal was recorded for 1000 sequential laser pulses with a window length of 2 μs using the *fast frame* function of the oscilloscope. The 98 μs of "dead" time between laser pulses was not recorded in order to reduce the record length. Nevertheless, transferring the record from the oscilloscope to PC for processing was the rate-limiting factor for imaging. The fast Fourier transform of

the signal was then calculated. The sidebands (D, Equation 17) were integrated over their bandwidth and summed to get one TAUM pixel.

Results and discussion

As a preliminary experiment to gauge the sectioning capabilities of TAUM, a small drop of whole, human blood was injected between two coverslips, separated with 190 μm spacers. The coverslips used in the experiment were 190 μm-thick glass coverslips. A small amount of refraction of the acoustic wave through the glass is expected, but no issues arose during the experiment to suggest this refraction to be problematic. After the blood had coagulated, axial depth scans were performed to obtain the axial profile of the sample with the imaging system.

For this lower-resolution experiment, the 0.3 NA objective was used to illuminate the sample. The back aperture of the lens was filled to produce a theoretical, diffraction-limited transverse resolution of 0.918 μm and axial resolution of 13.4 μm, given by the Rayleigh criteria described in [63]. The pulse energy at the sample surface was 180 nJ and 120 nJ in the pump and probe beams, respectively. The photoacoustic signals for this experiment were collected using the 6 MHz ultrasonic transducer.

Panel A of Figure 13 shows the depth-resolved, photoacoustic A-line of the blood sample using the off-axis PAM technique detailed in Chapter II. The axial resolution of this transducer, estimated as the speed of sound in tissue divided by the bandwidth of the transducer, is ~300 μm. Panel B shows the integrated photoacoustic signal as a function of depth. This measurement was obtained by integrating the 10 kHz

harmonic photoacoustic signals over the bandwidth of the transducer, while stepping the sample through the focus of the light. As can be seen in the figure, very little sectioning is obtained from the linear photoacoustic signal due to the large wings that are present far above and below the actual position of the sample. In fact, the sectioning in panel B is clearly worse than the photoacoustic A-line in panel A. Panel C shows a TAUM A-line as a function of depth. This panel shows a sharply peaked signal with no wings or background above or below the thrombus. Nominally, the axial resolution should be equivalent to the depth of focus of 13.4 μm. While this profile does not confirm the nominal resolution of the transient absorption technique, it does show that the TAUM profile has a much higher axial resolution than is possible if the signal was time-resolved, as is the case with traditional photoacoustic microscopy. The sharp edges of this profile suggest a higher resolution than that which can be directly inferred from the plot of the ~50 μm-thick thrombus.

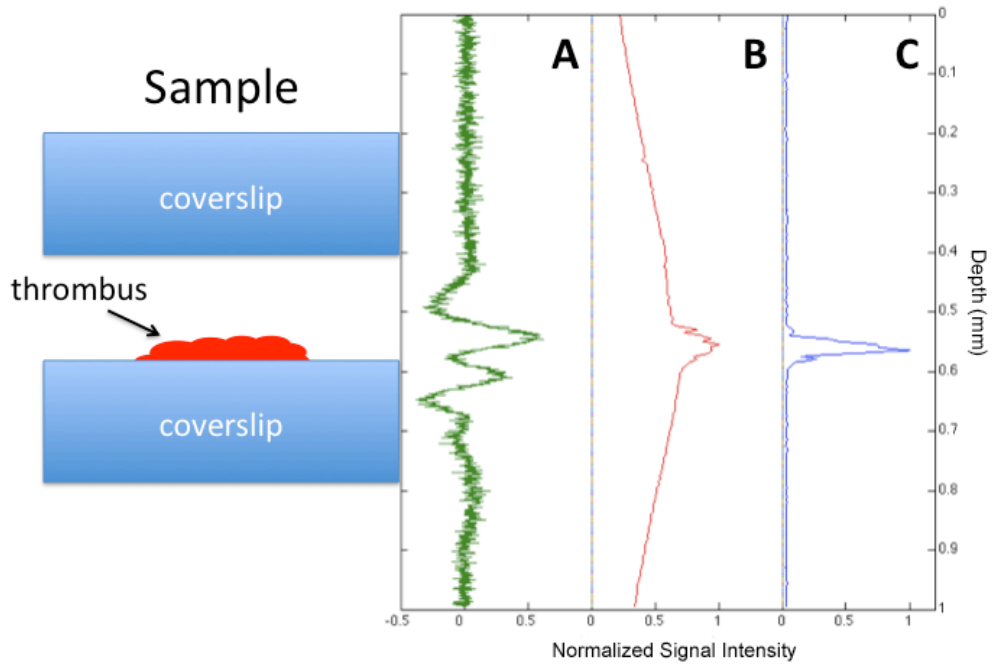

Figure 13. Axial scans through the thrombus sample. Cartoon of sample to left. A) Photoacoustic microscopy A-line. Nominal axial resolution is 300 µm. B) Integrated photoacoustic signal, analogous to single photon fluorescence microscopy. No axial sectioning ability. C) TAUM axial line, analogous to multiphoton microscopy. Nominal axial resolution is 7 µm (twice objective Rayleigh range).

A second experiment was performed to determine the relative signal to noise ratio (SNR) of TAUM compared to PAM. The SNR (defined as the peak signal divided by the standard deviation of the noise) was measured and compared in a sample of whole blood. The total average power on the sample was ~3 mW in both cases. One thousand pulses were used to generate the signal for both TAUM and PAM. In the PAM case, the time-domain signal was simply averaged over 1000 laser pulses. The results of these measurements yielded a TAUM SNR of 3019 and a PAM SNR of 643. This was a surprising result, given that the TAUM signal strength should be much smaller than the

PAM signal strength. The explanation lies in the noise portion of the SNR equation. The variance of the noise should be proportional to the detection bandwidth. The detection bandwidth for PAM is effectively the transducer bandwidth, which is 4.78 MHz for the 6 MHz transducer. The detection bandwidth for TAUM is the total bandwidth of the sidebands used to generate the TAUM pixel, or 3.4 kHz for the experimental conditions. We believe the ~1000 fold difference in detection bandwidth is what leads to the superior SNR of TAUM in this experiment.

As a first demonstration of TAUM imaging in a biological sample we have imaged capillaries in the cheek pouch of a Syrian hamster. For this experiment, cheek pouches were excised from freshly sacrificed Syrian hamsters. A 0.8 NA objective was used to produce a theoretical diffraction-limited transverse resolution of 0.344 μm and axial resolution of 1.87 μm. The pulse energy on the surface of the tissue was measured to be 140 nJ and 80 nJ in the pump and probe, respectively. The splitting ratio of the pump and probe beams in this experiment differ by 7.2% from the previous experiment. This discrepancy could be due to the use of different mirrors when the system was rebuilt between experiments or angle dependences in the beam splitters. The 25 MHz ultrasonic transducer was used to collect these images to take advantage of its increased bandwidth over the 6 MHz transducer used in the previous experiment. Since the transducer center frequency is not matched to the laser repetition rate, wider bandwidth leads to the measurement of more harmonics of the laser repetition frequency. Figure 14a shows the time-resolved photoacoustic B-scan of the capillaries in the cheek pouch. There appear to be 2 capillaries in the B-scan image; however, since the axial resolution

is so poor, little else may be gleaned from the image. Figure 14b shows a 300-μm portion of the B-scan in Figure 14a, centered around the capillaries. The extracted portion was stretched in the axial dimension to provide a 1:1 scale with the 100 μm x 100 μm TAUM image, which is shown in Figure 14c. Figure 14c shows a cross-sectional TAUM image clearly resolving 3 capillaries in the hamster cheek pouch. The capillary at the right edge of the image was not apparent in the B-scan. The largest feature in the image is ~10 μm, which is consistent with the diameter of red blood cells. Two of the capillaries in the cross-section are elliptical, which is a result of the red blood cells not being oriented normal to the image plane.

It is important to note that the TAUM image was taken with a transducer that has a nominal axial resolution of 150 μm in the off-axis configuration, which is larger than the entire field of view of the image. While the theoretical axial resolution has not been explicitly demonstrated, Figure 14c shows a minimum axial feature of 6 μm (FWHM), which is a 25-fold improvement over the axial resolution available from the single photon photoacoustic signal and over a factor of 2 better than any single photon photoacoustic microscope reported in the literature. The TAUM image in Figure 14c is under-sampled (2 μm x 2 μm) in both the lateral and axial dimensions. This is due to the imaging speed restrictions imposed by the oscilloscope used to collect the TAUM signals; however, this image clearly demonstrates the increased sectioning ability of the transient absorption technique.

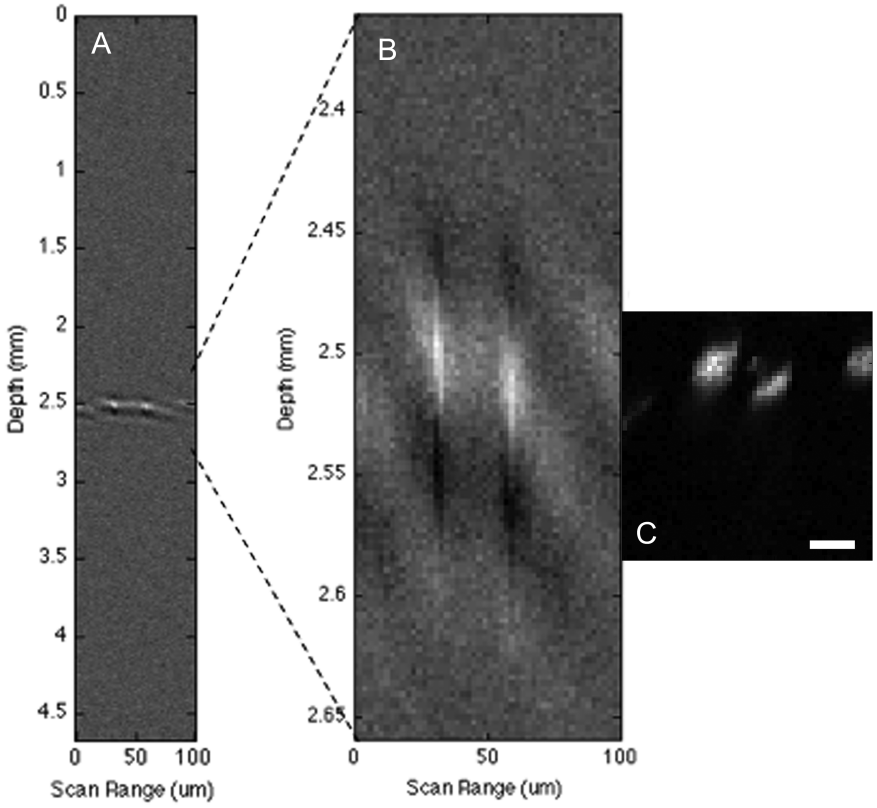

Figure 14. *Ex vivo* images of capillaries in the cheek pouch of a Syrian hamster. A) Photoacoustic B-scan (cross-section) of capillaries. B) 300 µm inset of B-scan to display 1:1 ratio with TAUM image. C) TAUM image of capillaries (cross-section) showing 3 capillaries of varying orientations. The scale bar is 20 mm.

The primary drawback to using this frequency domain collection technique is the cost on imaging speed. The photoacoustic emission from a number of laser pulses must be collected in order to perform the frequency domain analysis noted above to extract the TAUM signal. For the experiments outlined in this paper, 1000 laser pulses are used for each pixel. In Fig. 14c, the maximum SNR is ~ 200. Clearly, we could afford to sacrifice some of the SNR by reducing the number of laser pulses to improve imaging speed.

The imaging speed of the current system (~0.5 Hz) is limited by the collection speed of the oscilloscope used to collect and digitize the signals, rather than the number of laser pulses. With a better A/D card, the imaging speed would only be limited by the repetition rate of the laser. Therefore, for the same number of collection cycles, the imaging speed could be increased to ~10 Hz. This 20-fold increase would put this system's imaging speed on par with current photoacoustic microscopes boasting comparable lateral resolution. [45] However, it is important to note that due to the high resolution in the axial dimension, two-dimensional images will require two-dimensional scanning, as will be the case with any photoacoustic system utilizing highly focused excitation light.

The imaging speed may be further improved by integrating a higher repetition rate laser. Actively Q-switched lasers with similar or shorter pulse duration to the laser used in this study are commercially available with repetition rates up to 100 kHz. Utilizing these types of lasers would allow for increased speed or SNR, depending on the requirements of the application. While using higher repetition rate lasers will allow faster imaging speeds, the benefits are not limitless. As the pulse repetition period approaches the state recovery time (τ in Equation 13), the ground state population will not entirely recover between laser pulses, effectively diminishing the TAUM signal. A laser source with a pulse repetition rate of 100 kHz (10 μs period) should work well for molecules with $\tau < 3$ μs.

Potential tissue damage is always a concern for high resolution imaging due to tight focusing, especially for techniques that deposit energy into the tissue. We can use

the ANSI standards for the safe use of lasers as a guide. The ANSI standards specify the maximum surface fluence. At a tissue imaging depth of 100 μm in the Syrian hamster, the surface fluence (combined pump and probe) was 4 mJ/cm^2. The ANSI maximum permissible exposure is 20 mJ/cm^2 for visible light. At an imaging depth of 100 μm, the fluence used here is at least a factor of 5 below the ANSI limit. The maximum optical fluence at the focal plane was 42.7 J/cm^2, assuming no optical losses in the tissue. While the maximum fluence is high, it is within an order of magnitude of the fluence used in recent single photon photoacoustic studies [46]. During the experiments there were no visible signs of tissue damage. It is clear from the SNR in the TAUM image (Figure 14c) that the optical pulse energy could be reduced significantly, while maintaining acceptable SNR. Additionally, optimizing transducer parameters (larger transducer element size and NA for increased sensitivity) will significantly reduce the required fluence for this technique.

Conclusion

In conclusion, a novel imaging technique has been developed combining the exquisite spatial resolution afforded by non-linear microscopy with the superior penetration depth and molecular contrast inherent to photoacoustic imaging. The result, Transient Absorption Ultrasonic Microscopy, has been used to image microvasculature in the hamster cheek pouch, exhibiting axial resolutions in the range of 1-5 μm. This work represents the first time that axial resolutions less than 15 μm have been

demonstrated in photoacoustic microscopy. These results suggest that TAUM has the potential for cellular/subcellular resolution imaging.

Second-generation TAUM: optimization of speed and sensitivity

This section of Chapter III will discuss a second-generation TAUM system in which significant improvements to both speed and sensitivity are realized through hardware optimization.

Introduction

Photoacoustic microscopy (PAM) is an absorption contrast imaging technique that has seen rapid growth in recent years. PAM harnesses the photoacoustic effect; in which pulsed optical excitation induces molecular vibrations in a chromophore, leading to rapid thermoelastic expansion and the emission of a pressure wave. The pressure wave can then be detected with an ultrasound transducer, providing depth information about the chromophore through the time-of-flight measurements of the recorded ultrasound signal. PAM has been used to image many endogenous and exogenous chromophores in biology, such as hemoglobin [7], melanin [8], DNA/RNA [9], gold nanoparticles [10], and fluorescent dyes [11].

The point spread function of PAM is limited by the ultrasound transducer bandwidth in the axial dimension and either the focusing of the ultrasound transducer or the focusing of the excitation beam in the transverse dimension, depending on which implementation of PAM is used. In the former implementation, unfocused light is shone

on the sample and the signal localization is achieved solely through the focused transducer parameters. This results in axial and transverse resolutions in the 10s of microns at penetration depths up to centimeters [28]. In the latter, optical resolutions on the order of one wavelength of light can be achieved in the transverse dimension [29, 64]; however, the axial resolution is still limited to 10s of microns. The resulting asymmetric imaging voxel is the primary reason most PAM images are published as maximum amplitude projections (MAPs), with most of the depth information thrown away. This problem of asymmetry prompted our development of a method to obtain wholly optically resolved voxels. The result was transient absorption ultrasonic microscopy (TAUM) [65].

Transient absorption (TA) is a multiphoton process often used in spectroscopy to characterize chromophores by molecular signatures. TA measurements consist of a pump pulse and a probe pulse, separated in time by an interpulse delay. The pump pulse partially populates the excited state of the molecule and the probe pulse immediately follows, interrogating the ground state population. By observing the change in signal of the probe with the pump present and absent, information about the electron dynamics of the molecule may be directly measured. Through this technique, two primary physical properties may be obtained: transient absorption spectrum and ground state recovery time. When used in an imaging configuration, as is the case in TAUM, TA introduces improved optical depth sectioning equivalent to that in two-photon excited fluorescence and confocal microscopy. This is due to the fact that TA is a two-photon process and the

signal is a product of the pump and probe pulse power, resulting in an intensity-squared dependence. These concepts are discussed in detail in the preceding section.

The first generation (G1) TAUM system was designed as a proof-of-principle system. The initial prototype succeeded in demonstrating the improved axial sectioning of TAUM and showed, briefly, its imaging potential. However, the imaging system had one primary drawback: speed. Due to the hardware used and amount of processing required, the pixel rate of the G1 system was ~0.5 Hz. As such, even a simple 2D image took hours to acquire. For this reason, a second generation (G2) TAUM system was designed with a primary objective of increased speed.

In developing the G2 TAUM system, three primary areas were the focus of improvement for speed optimization: laser repetition rate, scanning speed, and processing. The laser repetition rate was easily increased through the purchase of a new laser. Implementing a galvanometer pair instead of stage scanning increased the scanning speed to the point that it would not bottleneck the speed of the system. The processing was the largest bottleneck of the G1 system. In order to improve this bottleneck, all of the processing for the TAUM signal extraction was implemented on a field programmable gate array (FPGA).

FPGAs are comprised of billions of transistors wired in such a way that allows reconfigurable logic on a single board via changes to firmware. As discussed in Chapter I, FPGAs can be found in many bio-imaging applications and result in vastly improved computational speed. The primary reason for this is the ability for a FPGA to parallelize many algorithms, allowing simultaneous calculations to speed up the processing time.

Methods and materials

The optical setup for the G2 TAUM system is a modification of the original TAUM system described previously. Figure 15 shows the system schematic. A frequency doubled Nd:YLF (Advanced Optical Technologies, Inc.) laser operating at 532 nm was used as the source. This source was chosen for its short pulse duration (0.6 ns) and ability to actively q-switch from single shot to 100 kHz. The output of the laser is split by a 50/50 beam splitter, forming the pump and probe beams. The pump beam passes through the beam splitter, while the probe beam is reflected into a short (~1 ns) optical delay arm. Another 50/50 beam splitter then recombines these beams after they are amplitude modulated at separate frequencies using a dual frequency optical chopper. The beams are frequency encoded so their contributions can later be extracted using Fourier domain analysis. The recombined beams are then sent through a galvanometer scanning mirror pair and a telecentric lens system with a magnification of 3x before being focused through a 0.8 NA water immersion objective lens (Olympus, Inc.) onto the sample.

The frequency encoded photoacoustic emission is collected using a 5 MHz immersion ultrasound transducer (NA = 0.23) in off-axis detection geometry as described in [50]. The imaging beam is scanned inside the focal spot of the transducer, so no mechanical scanning of the transducer is needed. For depth scanning of the sample a motorized stage (Newport Corp.) is used. The transducer signal is amplified by two RF amplifiers and then routed to the input of an 80 MHz digitizer front-end adapter module

connected to a field programmable gate array (FPGA) FlexRIO board (PXIe-7965R, National Instruments, Inc.).

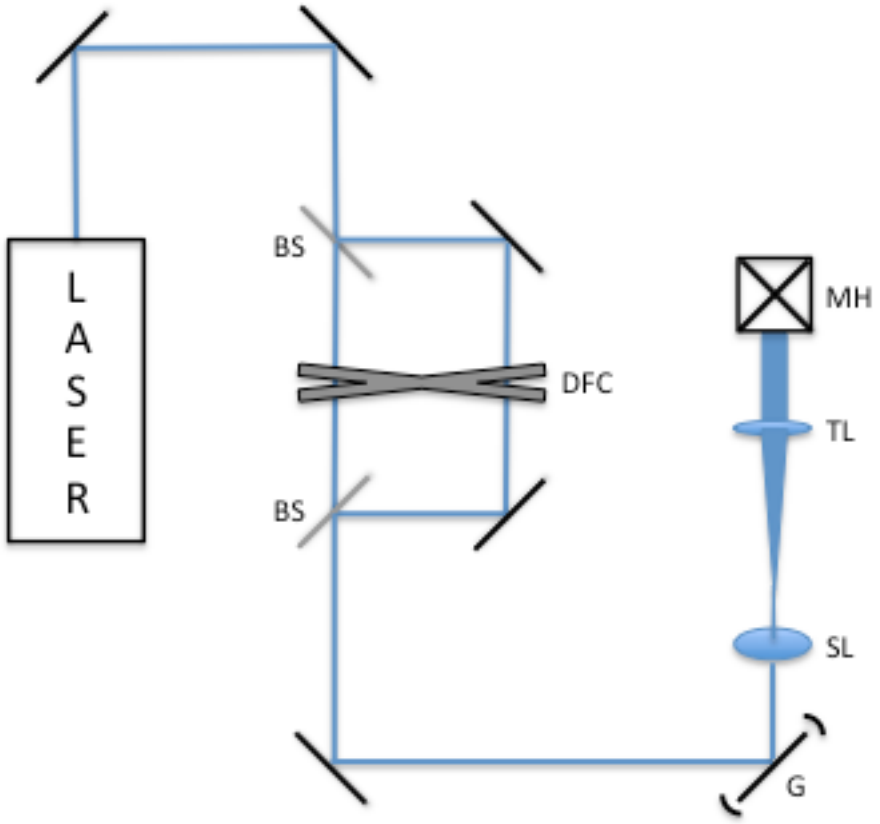

Figure 15. Schematic of the G2 TAUM system. BS: 50/50 Beam splitter, DFC: Dual-frequency optical chopper, G: Galvanometer scanning mirror pair, SL: Scan lens, TL: Tube lens, MH: Microscope head.

While the TAUM processing is explained in depth in the previous section and in [65], it will be summarized in this section and its implementation onto the FPGA will be described. The frequency encoding of the pump and probe illumination and subsequent frequency mixing when the beams interact in the sample results in the generation of

many narrow frequency bands, some of which are exclusive to the TAUM multiphoton signal. In order to extract these bands, Fourier domain analysis is performed. Many (typically 128) photoacoustic A-lines are taken at a single spatial point in order to collect a large enough time window to obtain sufficient spectral resolution. These A-lines are collected at the digitizer and passed directly to the FPGA board as a concatenated array of 32768 samples. The FPGA then computes a fast Fourier transform (FFT) on the array, yielding the spectral components. Once the spectrum is obtained, a pre-made binary mask designed to select only the frequencies of interest is applied to the 'enable' input of an accumulator, where the sum input is the spectrum array. This operation results in a single summed value of all frequency bins corresponding to the TAUM signal at that spatial position. This single value is then transferred to the host computer for display and data logging. Since the FPGA is capable of parallelizing the computation of the FFT, the speed bottleneck now becomes the laser repetition rate. At 100 kHz repetition rate and 128 A-lines per TAUM pixel, the ideal pixel rate (ignoring scanning flyback) is 780 Hz, more than three orders of magnitude improvement over the first generation system.

One of the greatest benefits of TAUM is increased depth sectioning capabilities. Unlike PAM, its axial resolution is not governed by the transducer bandwidth. Rather, the axial resolution is roughly approximated as the depth of field of the objective, as is the case in confocal microscopy and many multiphoton imaging techniques. This allows TAUM to enjoy the benefit of a low frequency transducer (minimal acoustic attenuation in tissue/water), while not suffering from decreased axial sectioning. If the current TAUM setup was used in PAM mode (5 MHz transducer, 45 degrees off axis), the axial

resolution would be 310 μm. The theoretical axial resolution, defined as full width at half maximum (FWHM), of the TAUM system according to the Rayleigh criteria described in [63] is 1.41 μm.

In an effort to verify the theoretical sectioning capabilities of the TAUM system, a cross-sectional image of a single red blood cell was taken. A single depth scan through the center of the RBC, which is ~1 micron thick was used to approximate the resolution of the system. Figure 16 shows the resulting profile of the scan, along with a Gaussian fit. The full width at half maximum (FWHM) of the Gaussian fit is 1.5 μm, which matches well with the theoretical value.

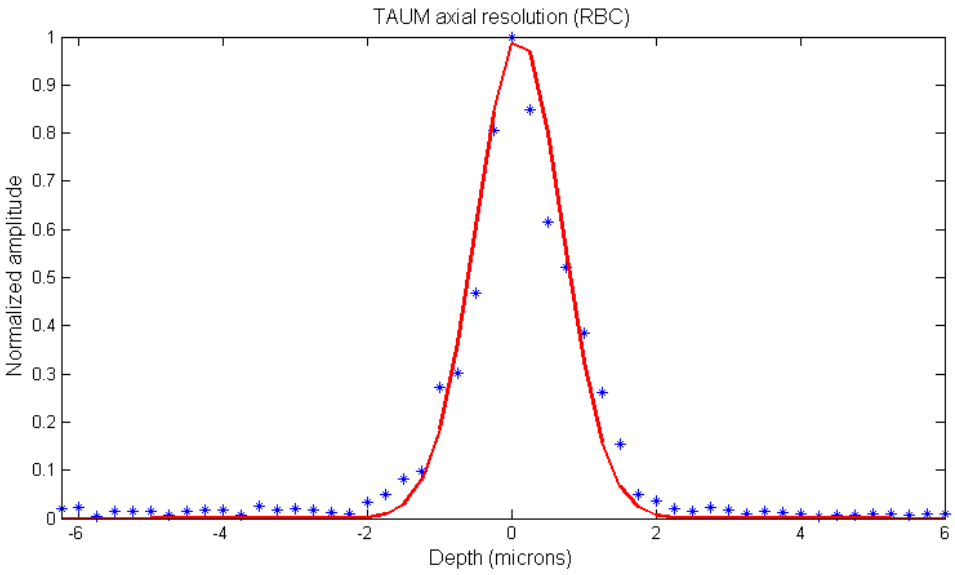

Figure 16. Axial profile through bi-concave center of a single red blood cell. Dotted line corresponds to data points taken using the TAUM system, while solid line is Gaussian fit curve. The FWHM of the fit curve corresponds to 1.5 microns.

Results and discussion

Having validated the theoretical sectioning capabilities of TAUM, two-dimensional scans were then taken. A blood smear was prepared using whole bovine blood and fixed to a glass slide with 95% methanol. The blood smear was imaged in both the *en face* and cross-sectional planes using the TAUM system. Pulse energy of 5 nJ was used for both the pump and probe pulses, resulting in 10 nJ of incident pulse energy on the sample at a pulse repetition rate of 50 kHz.

Figure 17a shows an *en face* image of erythrocytes on the blood smear. Note that this is not a maximum amplitude projection (MAP) image, as is typically shown in the field of photoacoustic microscopy, but a true slice as would be expected in confocal or two-photon excited fluorescence microscopy. This fact is evident in the image by the fact that some of the RBCs appear donut-shaped, while some appear as full circles of signal. A cross-sectional (b-mode) image of a single RBC can be seen in Figure 17b. Distortion of the RBCs during the fixing process is observed in this image, as the cell looks slightly dome-shaped. The edges of the bi-concave cell are cross-linked to the slide, while the center of the cell bulges up away from the slide, producing a meniscus-shaped structure.

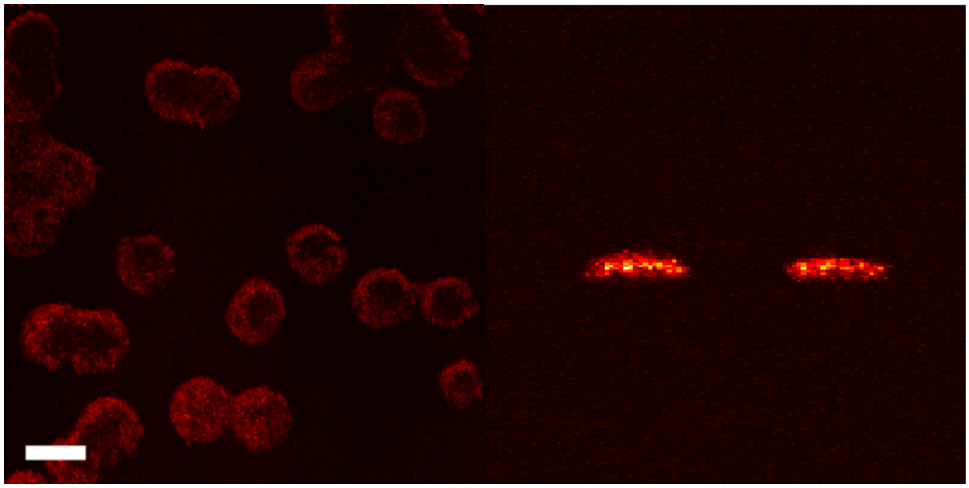

Figure 17. TAUM images of a blood smear. (a) *En face* image of single red blood cells on a slide, with characteristic "donut" shape apparent. Scale bar = 10 microns. (b) Cross-sectional image of two red blood cells on a slide. Slide distortion of the cells due to fixation is evident in the meniscus shapes of the cells.

Most of the improvements on the first generation TAUM system were designed to provide increases in imaging speed. These improvements allow for up to ~ 400 Hz pixel rates, which is a factor of 1000 improvement over the previous system. This not only made two-dimensional imaging much more robust, but allowed for volumetric imaging. The above 200x200 pixel images were taken in less than two minutes. A volumetric rendering of several RBCs is shown in Figure 18. The dimensions of the volume are 50x50x20 μm. To the best of the author's knowledge this is the first time photoacoustic microscopy has been used to fully resolve RBCs in a volumetric image.

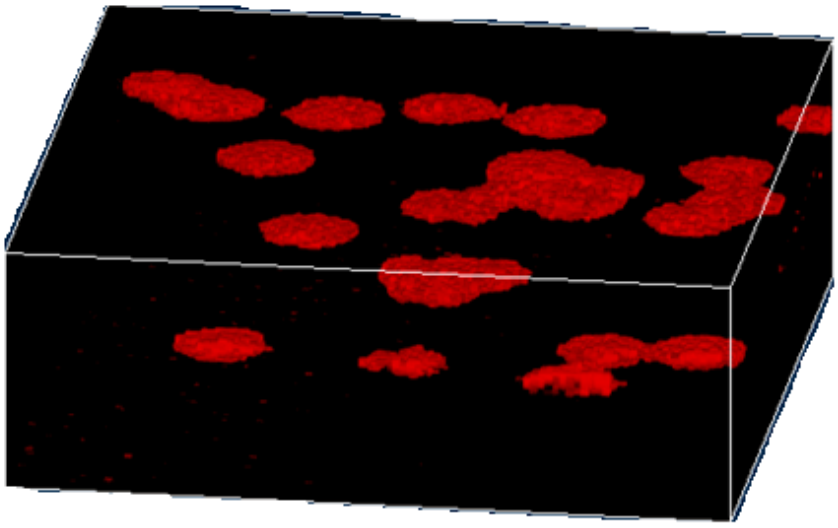

Figure 18. Volumetric rendering of red blood cells fixed on a slide. Volume dimensions are 50x50x20 microns.

After successful imaging of the fixed RBCs, an *ex vivo* biological sample was imaged. Freshly sacrificed, stage-6 chick embryos were obtained and the embryos were removed from their shell and placed into a petri dish to be imaged using the TAUM system. Chick embryos have a rich and complex vasculature throughout the chorio-allentoic membrane, which is used to nourish the embryo during development. Figure 19 shows *en face* (a) and cross-sectional (b) images of individual RBCs inside the small vessels in the embryo. The subcellular resolution of TAUM is able to depict the individual cells of varying orientation in both images. Bifurcations off of the primary vessel in the image can be seen in Figure 19a. The cross-section in Figure 19b was taken through the dotted line depicted in Figure 19a. While TAUM is currently not fast enough

to image these cells as they move through a live organism, future improvements to TAUM may enable such a feat.

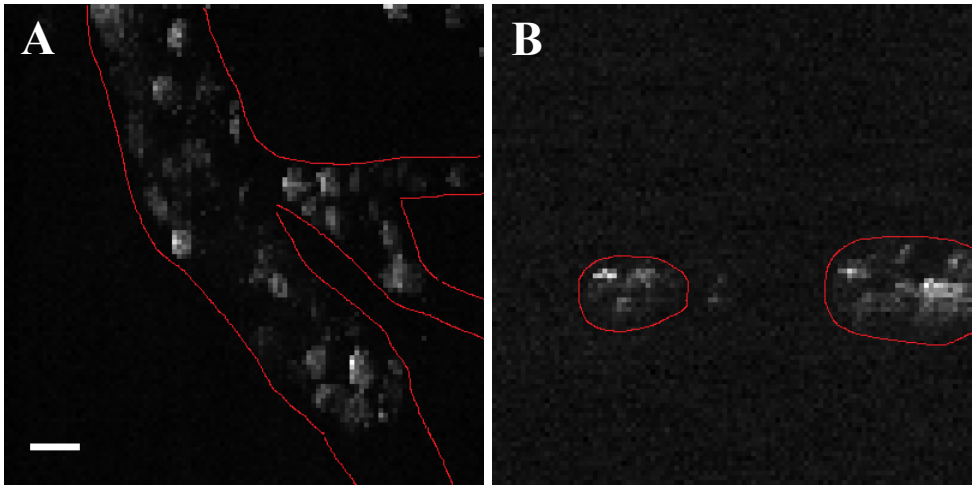

Figure 19. Transverse and axial slices through a vessel network in an *ex vivo* embryo. (A) Transverse TAUM image of individual RBCs inside a bifurcated vessel structure. (B) Axial TAUM image through the dotted line shown in (A). Cross-sections of individual cells inside the lumen are present. Scale bar = 10 microns. Note: red lines indicating possible lumen locations have been drawn for reference. These lines are only suggestions from the author to illustrate a possible scenario and may not indicate actual vessel structure.

While this manuscript has only reported findings for the chromophore hemoglobin, this technique could be used for high resolution, three-dimensional imaging of any biological chromophore, given the appropriate excitation wavelength. Other chromophores of future interest include melanin, myoglobin, and cytochrome-C. Imaging of cytochrome-C could provide label-free insights into metabolic processes.

The pulse energies used in this study were lower (in some cases significantly so) than many other high-resolution OR-PAM studies. Through improvements to the TAUM

design, the pulse energies needed for reasonable signal were reduced by a factor of 20-30 over the first generation results. While this is an excellent improvement, the fluence at the focus is still ~ 2 orders of magnitude larger than the ANSI limit for surface fluence in tissue. We have not witnessed tissue damage at this fluence level, but methods for further decreasing the fluence will be investigated in future studies. Increasing the number of pulses (A-lines) used for each TAUM pixel will allow a decrease in fluence, while maintaining a comparable signal-to-noise ratio.

Although the imaging speed of this second generation TAUM system has been greatly improved over past implementations, it is still a relatively slow technique when compared to other nonlinear microscopies, such as TPEF and CM. In order to further improve the speed of the system, optimizations to the FPGA code will need to be made to provide linear speed benefits above 50 kHz. Currently, while the speed increases with increasing repetition rate above 50 kHz, the returns are diminishing. With proper code (and possibly hardware configuration) optimizations, the speed could be increased as a linear function of laser repetition rate, ushering in great returns as q-switched laser technology advances to higher repetition rates. Additionally, lowering the number of pulses used for each pixel can increase imaging speed. Currently, 128 pulses are used per pixel, but 64 pulses per pixel have also been used with success. As in many imaging techniques, there is an obvious trade-off between speed and SNR.

Ultimately, the goal is to refine the technique to the point that a femtosecond Ti:Sapphire laser may be used. This would serve to increase the imaging speed dramatically due to the highly increased repetition rate of mode locked lasers. Using a

femtosecond laser would also provide much better temporal resolution for the transient absorption process, allowing greater control over the interpulse delay for measurements of ground state recovery time in molecules that would be inaccessible to a nanosecond source.

Conclusion

In conclusion, transient absorption ultrasonic microscopy (TAUM), a previously developed, high-resolution, label-free, molecular imaging technique has been greatly improved upon. Increases in imaging speed of up to three orders of magnitude have been demonstrated, while reducing pulse energies by a factor of 10-20. These optimizations enabled three-dimensional volumes of single red blood cells, demonstrating axial resolution of 1.5 μm. Additionally, the technique has been demonstrated *ex vivo* in a chick embryo, visualizing individual red blood cells inside small vessels in both the transverse and axial planes.

Differentiation of oxidized and reduced hemoglobin using TAUM

In this section of Chapter III, the second-generation TAUM system described above is used to differentiate oxidized and reduced forms of hemoglobin by measuring the ground state recovery time of each molecule. A well-known, well-characterized chromophore (Rhodamine 6G) is used to verify the recovery time measurements. Recovery times of oxy- and deoxy- hemoglobin are quantified and shown to be statistically different.

Introduction

High-resolution molecular imaging has become an important tool in biology and biochemistry. The ability to differentiate multiple chromophores on a cellular or subcellular level has the potential for great impact on the medical field. Optical molecular imaging is quickly becoming a valuable addition to traditional biopsy, because it can obtain much of the same information about the molecular species of interest, and it can do so noninvasively. Current molecular imaging techniques include, but are not limited to, multiphoton microscopy techniques such as two-photon excited fluorescence [66], second [17] and third [18] harmonic generation, coherent anti-Stokes Raman scattering (CARS) [20], and pump probe spectroscopy [21].

Chapter III introduced a new molecular imaging technique termed transient absorption ultrasonic microscopy (TAUM) [65], which combines photoacoustic microscopy with pump probe spectroscopy. The marriage of these techniques enables strong absorption contrast imaging with a spatial resolution equivalent to that of multiphoton and confocal microscopy. Additionally, TAUM provides access to important and unique molecular parameters that cannot be obtained through other imaging techniques. Measuring photoacoustic emission grants access to endogenous chromophores that do not fluoresce, such as melanin and hemoglobin, while the pump-probe configuration both improves the spatial resolution due to its two-photon dependence and allows measurement of molecular signatures such as the transient absorption spectrum and ground state recovery time. The transient absorption spectrum can be measured by varying either the pump or probe wavelength, while the ground state

recovery time can be measured by varying the interpulse delay, i.e. the time delay between the pump and probe pulses. The latter is analogous to fluorescence lifetime measurements.

Ground state recovery time is defined as the time it takes molecules to make their way back to the ground state after photoexcitation. This molecular parameter is chromophore and environment dependent and can be used to differentiate multiple chromophores much in the same way fluorescence lifetime is used to differentiate multiple fluorophores. This parameter has been measured using photoacoustic measurements in the past for long lived recovery times [67, 68]; however, in those studies the authors used time domain extraction of the pump-probe signals, which placed a fundamental limit on the achievable temporal resolution, because the pump and probe signals become indistinguishable once they begin to overlap in time. TAUM extracts the pump-probe signal in the frequency domain, separating the contributions of the pump and probe pulses by optically chopping each beam at different frequencies. This results in a temporal resolution equal to the pulse duration of the laser source, rather than the temporal bandwidth of the transducer.

Methods and materials

The system used to measure the ground state recovery times is modified from the original TAUM design. In the modified design, two Nd:YLF frequency-doubled, 532 nm lasers (Advanced Optical Technologies, Inc.) make up the pump and probe sources. These lasers have a 0.6 ns pulse duration and a maximum repetition rate of 100 kHz. The

schematic of the modified TAUM system can be seen in Figure 20. The two lasers are controlled externally using triggers sent from a computer through a digital pulse delay generator (P-400, Hiland Technologies). The pulse delay generator receives the master trigger (TTL pulse) from the custom built LabVIEW program, and then generates two more TTL pulses, each with a controllable delay from the master pulse. These two delayed TTL pulses are then used to trigger the lasers. In this configuration, the interpulse delay can be easily adjusted through a serial connection to the pulse delay generator. Jitter is not a problem at the time scales we are investigating, as the jitter from the lasers is ~ 200 ps and the jitter from the pulse delay generator is ~ 2 ps.

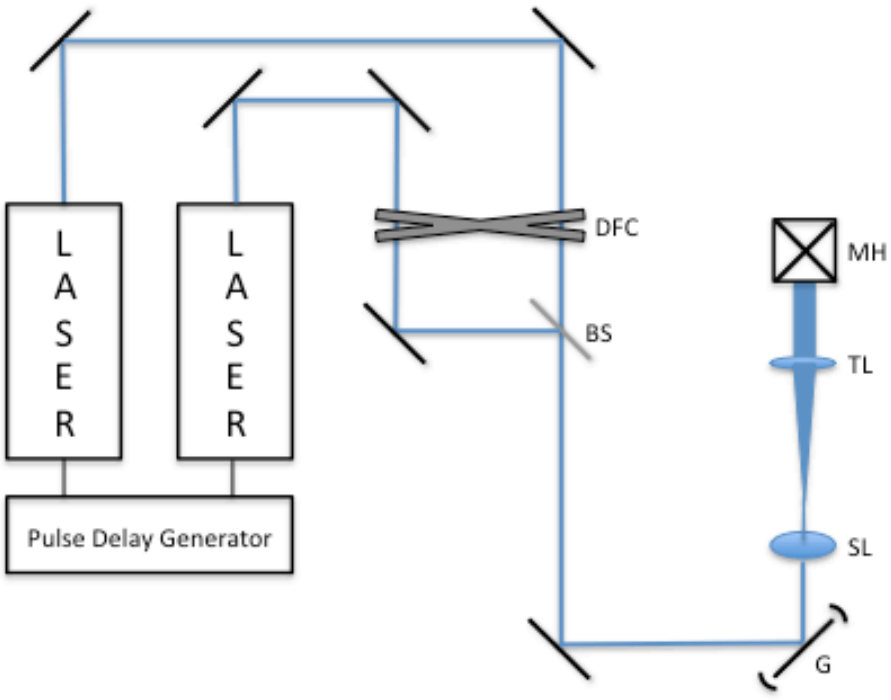

Figure 20. Schematic of TAUM system modified for measurement of ground state recovery time. DFC: Dual-frequency optical chopper, BS: Beam splitter, G: Galvanometer scanning mirror pair, SL: Scan lens, TL: Tube lens, MH: Microscope head.

In order to extract the TAUM signal, the pulses emitted from each laser are chopped at separate frequencies using a dual-frequency optical chopper. This process is described in detail previously in Chapter III. After optical chopping, the beams are combined using a beam splitter, then passed through a beam expander to achieve diffraction-limited spatial resolution and delivered to the sample through a 0.8 NA water immersion objective (Nikon, Inc.). After excitation, the photoacoustic emission is collected using a 6 MHz transducer (V-305, Olympus NDT) and amplified using two RF in-line amplifiers.

Each TAUM pixel is collected and processed in real-time using the FPGA configuration described in the previous section. This second-generation TAUM system is capable of pixel rates up to 500 Hz, a 1000-fold improvement over the speed of the initial prototype. The Fourier domain processing and filtering is performed on the FPGA in real time and a custom LabVIEW program synchronizes the delay generator sweep with the TAUM collection and processing.

Results and discussion

In an effort to verify the measurement of ground state recovery time via TAUM, a chromophore with known absorption and molecular relaxation properties was measured. Rhodamine 6G (R6G), a common laser dye, has a fluorescence lifetime of ~ 4 ns [69]. While the photoacoustic effect measures the non-radiative transitions rather than the fluorescence, the extremely high quantum yield (~95%) [70] of R6G dictates that the ground state recovery time will be dominated by the fluorescence lifetime. Therefore, we

will approximate the expected ground state recovery time to be no longer than 4 ns. For the purposes of these studies, 1/e lifetime will be estimated as the data point corresponding to 37% of the peak TAUM amplitude (at $t_d = 0$).

A 500 µM concentration of R6G was placed in a 200 µm ID capillary tube and the ground state recovery time was measured using the TAUM system. The average 1/e lifetime over 44 datasets was measured to be 3.34 +/- 0.65 ns, which agrees well with the expected lifetime of 4 ns. The discrepancy could be attributed to the fact that TAUM measures all electron relaxation paths, including the much shorter non-radiative transitions, while fluorescence only measures radiative paths. Figure 21 shows a plot of the ground state recovery time of R6G as measured by TAUM. The plot is an average of 10 measurements.

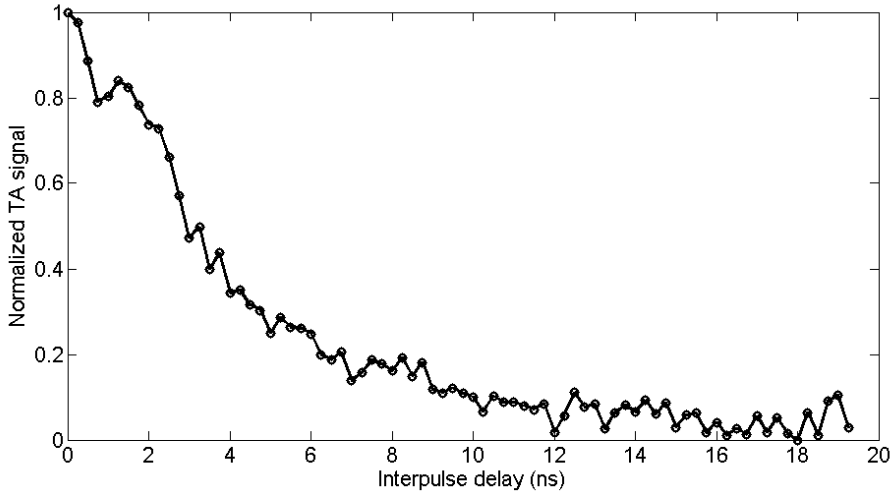

Figure 21. Ground state recovery time plot of Rhodamine 6G as measured by TR-TAUM. 1/e lifetime measured to be 3.6 ns.

After verifying the ability of TAUM to measure the ground state recovery time of a well-documented chromophore, the system was used to investigate whole blood. Blood has been shown in previous 532 nm degenerate pump-probe studies to have a ground state recovery time of ~ 9 ns [59]. However, these previous studies did not investigate the effects of oxygenation on the recovery time of blood. Whole bovine blood samples were prepared in a similar manner to the R6G samples described above and the samples were measured immediately after preparation. Figure 22a shows a representative recovery time plot of whole blood, which was left exposed to air before the sample was prepared, resulting in an oxygen saturation of > 95%. The plot is an average of 10 measurements. The average 1/e lifetime over 50 fully oxygenated whole blood samples was measured to be 3.73 +/- 0.82 ns.

Deoxygenated blood samples were then prepared using the technique described in [71]. Sodium dithionite, a commonly used reducer, was mixed with the blood to temporarily provide a 0% oxygenation blood sample. The sample remains completely deoxygenated for ~ 15 minutes before it gradually begins to re-oxygenate. All measurements for deoxygenated samples were taken within 10 minutes of sample preparation. Figure 22b shows a representative recovery time plot of the deoxygenated blood samples using 10 averages. The average 1/e lifetime over 44 samples was measured to be 7.9 +/- 1.01 ns. The data from oxygenated and deoxygenated blood shows a distinct difference in the ground state recovery time. The difference is illustrated in Figure 21c, which shows the normalized lifetime plots of oxy- and deoxy- blood. This

difference can be used in imaging to differentiate multiple chromophores or even to map oxygen saturation in a TAUM image with a single wavelength.

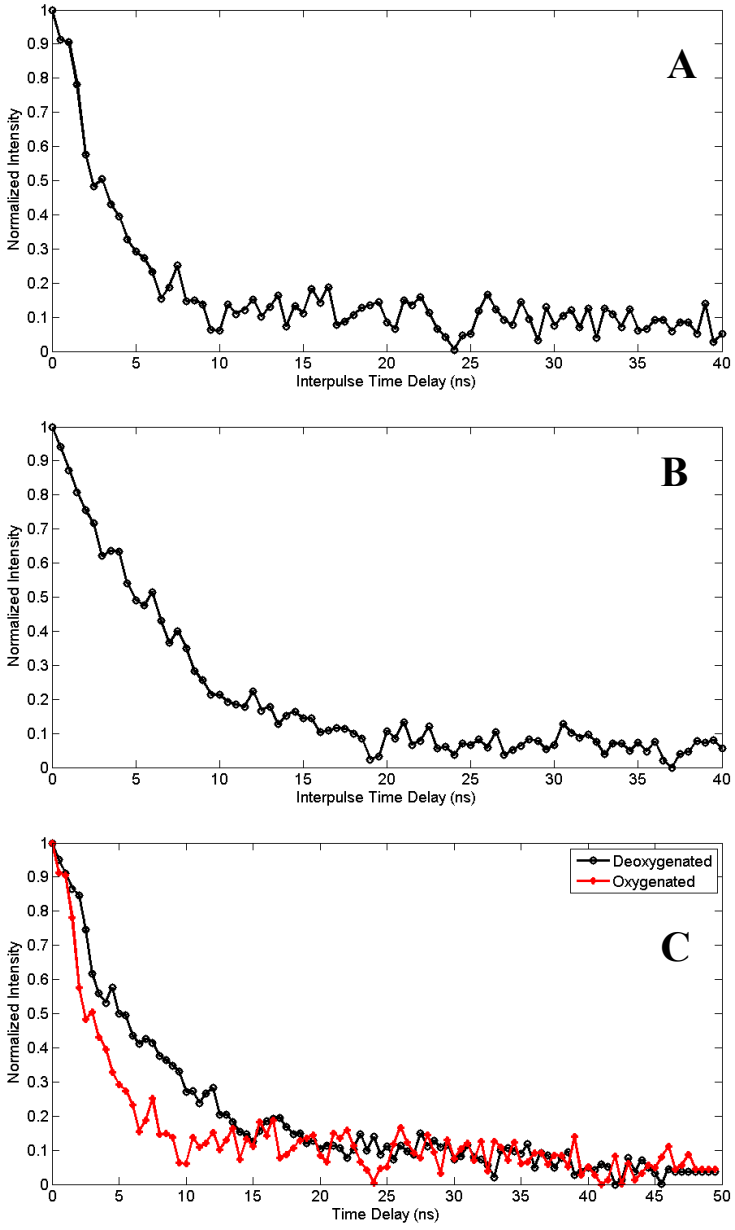

Figure 22. Ground state recovery time plots of oxygenated and deoxygenated whole bovine blood. (a) Recovery time of fully oxygenated blood (~ 4 ns). (b) Recovery time of fully deoxygenated blood (~ 8 ns). (c) Both recovery times plotted in overlay showing a clear difference in decay times.

Figure 23 shows a histogram of lifetime values of the three aforementioned chromophores. Each chromophore was measured at least 40 times (n=40). It is clear from the histogram that deoxygenated blood is clearly distinguishable from oxygenated blood and R6G and there is no overlap in the distribution. This is a good sign for future studies trying to measure SO2 in a TAUM image.

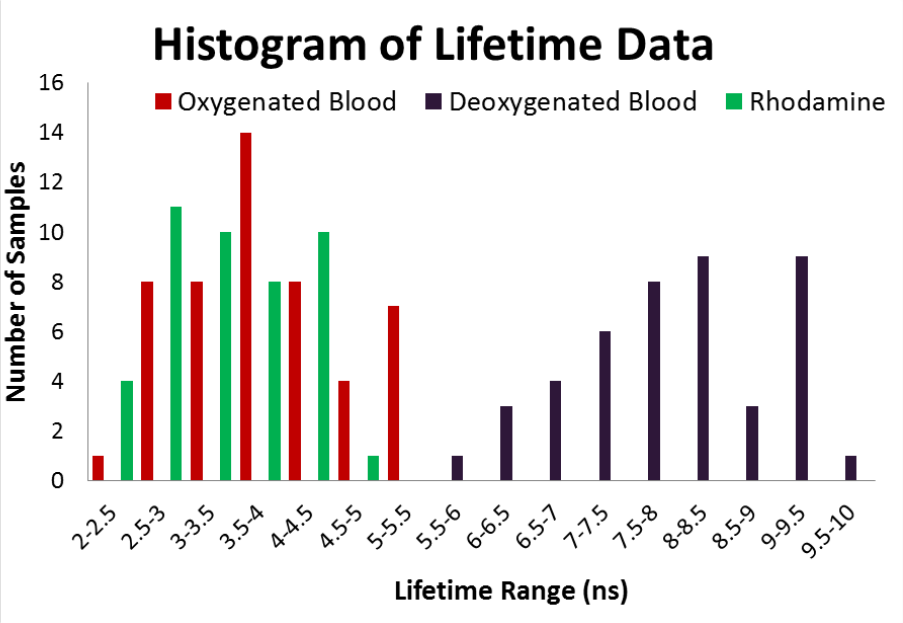

Figure 23. Histogram of ground state recovery times of oxygenated blood, deoxygenated blood, and Rhodamine 6G. The histogram plot shows no overlap between oxy- and deoxy- recovery time. Each chromophore was measured at least 40 times.

Since this technology would be best utilized by taking spatial images that have molecular specificity encoded into them (via ground state recovery time), one-dimensional image data was acquired while varying the interpulse delay. For this experiment, R6G was placed in a 50 µm ID capillary tube and subsequently imaged.

Figure 24 shows the resulting image, where the x-axis corresponds to spatial scan range (the image width is ~ 200 μm) and the y-axis corresponds to decreasing interpulse delay (-5 ns at the top of the image extending out to + 45 ns at the bottom of the image). The tube structure is clearly visible in the image. The bright band of signal near the top of the image corresponds to the peak at which the interpulse delay = 0. This band indicates the region in which the R6G solution is present. Note that this band does not run all the way across the tube structure. This is because there is strong boundary enhancement along the tube edges due to the large acoustic refractive index difference, so no dependence on interpulse delay is noted at these regions.

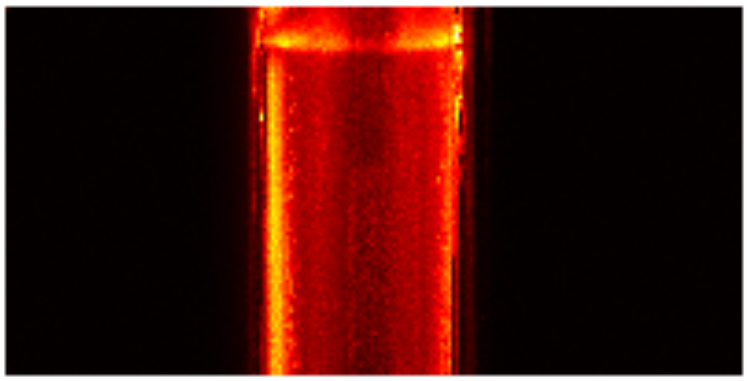

Figure 24. Two-dimensional TAUM image of a 50 μm ID capillary of R6G showing spatial distribution of ground state recovery time.

Finally, an effort was made to distinguish multiple chromophores in a single image. In order to demonstrate this, a phantom was created consisting of a 200 μm ID tube filled with R6G alongside a 200 μm ID tube filled with India ink. The tubes were imaged successively using the modified TAUM system and the interpulse delay was

changed between each image. Figure 25 shows a panel of images depicting *en face* scans of the phantom containing the two tubes. Beginning at the temporal overlap of the two pulses (interpulse delay = 0), at which the TAUM signal should be largest, the interpulse delay was then changed by 2 ns between each image, resulting in a total interpulse delay change of 16 ns.

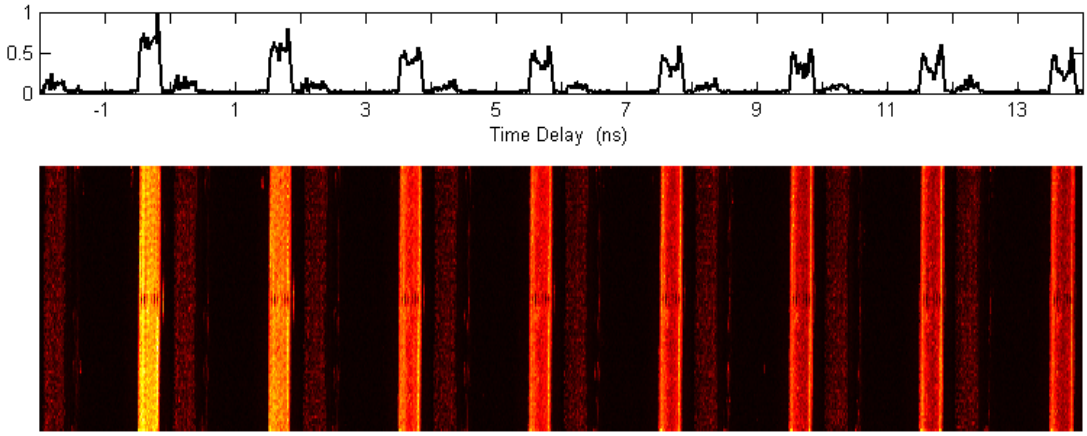

Figure 25. Panel of TAUM images showing relative dependence on interpulse delay in R6G and India ink.

The panel of images and accompanying plot shows exactly what is expected. The R6G signal, which has been shown to have a TAUM signal dependent on interpulse delay, gets weaker as the interpulse delay is increased, until it levels off (around the fourth image in the panel). The signal from the India ink, however, stays constant throughout all 8 images. This is also expected, as India ink has not been shown to have a measurable ground state recovery time at this timescale.

A more compelling application for this technology is the differentiation of oxygenated and deoxygenated blood in a single image. For this pilot study, statistical difference was found in the ground state recovery times of oxy- and deoxy- blood; however, differentiation of the oxidized and reduced forms will be the focus of future work. This is more difficult to achieve in phantoms due to the noisier signals measured in whole blood and the need for two individual blood cells of differing oxygenation to be present in the 1.5 μm axial imaging plane. Future studies may achieve this by moving to a weaker focusing objective to ensure blood cells of each type can be observed in a single image.

Conclusion

In conclusion, we have developed and demonstrated a modified TAUM setup capable of measuring ground state recovery times in the nanosecond range. The system was verified by measuring R6G, and was then used to measure ground state recovery times for oxygenated and deoxygenated blood. It was found that the recovery times for blood were highly dependent on oxygenation, with more than a factor-of-two difference in the characteristic recovery times of each. These results show promise for subcellular resolution oxygen saturation imaging in future TAUM research.

CHAPTER IV

CONCLUSIONS AND FUTURE WORK

In summary, the purpose of this work was to develop and characterize a multiphoton photoacoustic microscope. This design was focused on merging photoacoustic microscopy with transient absorption (pump-probe spectroscopy) for vastly improved sectioning and the introduction of molecular contrast. The need for such a microscope became apparent due to the poor sectioning capabilities of traditional photoacoustic microscopes because of the reliance on the transducer bandwidth for resolution. Chapter I describes the motivation for increasing the resolution, as well as the benefits of introducing molecular contrast to PAM.

Chapter II describes off-axis photoacoustic microscopy, which later became the foundation for the multiphoton photoacoustic microscope. In OA-PAM, the acoustic detection axis is separated from the optical axis by simply angling the detector toward the sample and positioning it roughly 15 - 45 degrees off of the optical axis. The primary benefit of this setup is the simplification of the design. It requires no custom components, in sharp contrast to co-axial PAM setups which require custom optics or special beam splitters to properly deliver the light and collect the acoustic waves along the same axis. A secondary benefit of OA-PAM is the quasi-dark field sectioning that is made possible by setting the transducer off-axis. This enhances the ability of the microscope to reject unwanted signals, which may overpower weaker signals of interest. The one compromise required for OA-PAM implementation is a modest reduction of

axial resolution equal to the reciprocal of the cosine of the detection angle. The imaging capabilities of OA-PAM are demonstrated by imaging black hairs embedded in chicken breast and through MAP images and volumetric vasculature reconstructions of a Syrian hamster cheek pouch. It is important to note that the simplification in OA-PAM allows for high quality, commercial objectives to be used in reflection geometry. This is the first time this had been possible in photoacoustic imaging. This became very important for the multiphoton microscope because exquisite focusing is required for suitable nonlinear excitation efficiency.

The latter part of Chapter II details and compares two proposed processing methods for photoacoustic microscopy: quadrature demodulation (QD) and Hilbert transform (HT) enveloping. Photoacoustic signals are bipolar, similar to ultrasound and MRI signals. However, unlike ultrasound and MRI, images taken with PAM are rarely processed, resulting in intensity "striping" in depth. This leads to a relatively poor reconstruction of the true morphology of the imaged structure. Enveloping techniques transform these bipolar signals into an accurate representation of the morphology of the sample. Raw, QD processed and HT processed A-lines and B-scans are shown taken from data from vasculature in the hamster cheek pouch. It is determined that both methods do an admirable job of reconstructing the expected morphology, although the HT method results in some bleed through of the modulation, resulting in "shoulders" on the axial PSF.

Chapter III describes the design and characterization of a multiphoton photoacoustic microscope. By merging PAM with transient absorption effects, all-

optical sectioning was achieved, while still detecting acoustic waves generated by thermoelastic expansion. The first section of Chapter III describes the physics and initial prototype of the transient absorption ultrasonic microscope (TAUM). The increased axial sectioning is demonstrated on a blood sample and compared to the traditional PAM signal with obvious success. The TAUM system is then used to take cross-sectional images of single capillaries in a hamster cheek pouch. This was the first time a capillary had ever been depth resolved using photoacoustic imaging.

The next section of Chapter III describes a second iteration of the TAUM system in which the speed and sensitivity were vastly improved. Hardware improvements such as a laser with a faster repetition rate, galvanometer scanning mirrors, and field programmable gate array hardware for real-time processing enable up to 1000-fold improvement in pixel rate over the initial prototype. The second-generation system is characterized by imaging single red blood cells (RBCs) on a microscope slide. The axial resolution is measured to be ~ 1.5 μm. A volumetric reconstruction of the RBCs is also demonstrated. Finally, *en face* and cross-sectional images of RBCs in the vasculature of a chick embryo are demonstrated. This work represents the first time single RBCs have ever been fully resolved using photoacoustic imaging.

The last section of Chapter III details the molecular contrast capabilities of TAUM. Ground state recovery time is defined as the time it takes for electrons to make their way back to the ground state after photoexcitation. Ground state recovery time measurements are enabled by modifying the TAUM setup to include a second laser and controlling the delay between the pulses of each laser. Then, by mapping the TAUM

intensity at varying interpulse delays, the ground state recovery time can be directly measured. This technique is first demonstrated on Rhodamine 6G (R6G), a well-documented chromophore. The measured ground state recovery time using TAUM is 3.3 ns, which matches reasonably well with the published fluorescence lifetime of ~ 4 ns. Once the ability of TAUM to measure the ground state recovery time of a known chromophore was validated, measurements were taken on the oxidized and reduced forms of hemoglobin in whole blood. A minimum of 40 separate datasets for each chromophore (oxidized and reduced hemoglobin and R6G) was taken to ensure statistical significance. The ground state recovery time of oxy- and deoxy- hemoglobin as measured with the TAUM system is 3.65 ns and 7.9 ns, respectively. These results suggest that future iterations of TAUM could be used to measure oxygen saturation with a single wavelength, instead of having to rely on the current spectroscopic methods.

Future work concerning the OA-PAM system should include characterization and imaging with a second generation OA-PAM system. This work has already been started and looks very promising. By using a high frequency (27 MHz -6 dB bandwidth) polymer transducer with a long focal length, high resolution, large field of view volumes may be taken using the OA-PAM configuration. Galvanometer scanning can still be achieved by moving the transducer closer to the sample. This places the sample out of the focus of the transducer, thus resulting in some loss of SNR, but the benefit of galvo scanning while maintaining a large (3mm+) field of view is immense. OA-PAM scanning at A-line rates up to 100 kHz has already been demonstrated, obtaining a volume of a hair phantom (three hairs crossed) with a field of view up to 2mm and depth

of field of up to 3 mm has been demonstrated. Figure 26 shows a MAP image generated from a volumetric rendering of the hair phantom, taken with the second-generation OA-PAM system. The hairs in the image can be seen across a depth of 3 mm. These results are very promising for future OA-PAM work.

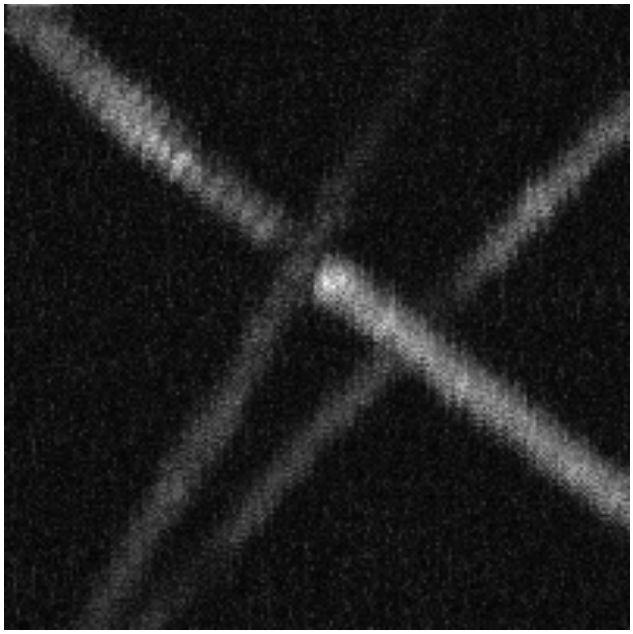

Figure 26. MAP image of a 3-hair phantom taken using the second-generation OA-PAM system. Image dimensions are 2 mm^2 and signal from the hairs can be observed simultaneously across a depth of 3 mm.

Precise and quantitative characterization of the resolution, depth of field, field of view and SNR of the improved system should be completed, followed by imaging of applicable targets. Whole-body embryo imaging would be an excellent first trial. Zebrafish embryos and Xenopus tadpole spawn have interesting and extensive vasculature, as well as a great deal of pigmentation, both of which should be easily

imaged by the second generation OA-PAM system. In some cases, it may be necessary to treat the embryos with a pigment blocker, as is done in [72] for optimized imaging of vasculature.

The second-generation OA-PAM system has also incorporated an FPGA and real-time processing of the PAM A-lines by quadrature demodulation, as discussed in Chapter II, has already been implemented. This allows for real-time, processed data, representing the chromophore spatial distribution in the sample with much greater accuracy in depth than other competing research, such as the work done in [73]. Initial data has already been taken to prove the validity of the quadrature demodulation algorithm using the second-generation system. As Q-switched laser technology improves and higher repetition rates are available, this system should scale easily with new, cutting edge technology, allowing for A-line rates approaching those found in ultrafast optical coherence tomography (OCT) systems [74-77]. Eventually, real-time volumetric PAM imaging will be realized.

Future work concerning the TAUM system should include optimizing FPGA algorithms to make full use of the repetition rate of the laser, investigation of other chromophores, such as Cytochrome C or myoglobin, and investigation of *in vivo* models for angiogenesis, such as nude mice. Efforts to further increase speed though optimization of pulses per pixel should also be studied.

Long term goals should include optical detection of the acoustic waves and utilizing a picosecond or femtosecond pulsed laser source to improve the temporal resolution of TAUM. Optical detection of the acoustic waves will enable non-contact

photoacoustic imaging, a goal that is a hot topic in the field right now. This would rid the system of constraints such as field of view limitations due to the need to scan inside the detector focus and geometry/location limitations due to the need to water couple to the transducer. Moving to a picosecond or femtosecond source would provide multiple tangible benefits. First and foremost, it would allow for the measurement of ground state recovery times for a much larger pool of chromophores than the current system can access. Many other biological chromophores, such as melanin, have been shown to exhibit lifetimes of 10s of picoseconds, which is not measurable with the current source due to the longer (600 ps) pulse duration. Additionally, since picosecond and femtosecond lasers are mode-locked, the conceivable repetition rates are much higher. This would potentially allow for much faster TAUM measurements.

REFERENCES

1. B. N. Giepmans, S. R. Adams, M. H. Ellisman, and R. Y. Tsien, "The fluorescent toolbox for assessing protein location and function," Science **312**, 217-224 (2006).
2. R. Weissleder and U. Mahmood, "Molecular imaging," Radiology **219**, 316-333 (2001).
3. C. H. Contag and M. H. Bachmann, "Advances in *in vivo* bioluminescence imaging of gene expression," Annual Review of Biomedical Engineering **4**, 235-260 (2002).
4. P. J. Jiang and Z. J. Guo, "Fluorescent detection of zinc in biological systems: recent development on the design of chemosensors and biosensors," Coordination Chemistry Reviews **248**, 205-229 (2004).
5. V. Ntziachristos, C. Bremer, and R. Weissleder, "Fluorescence imaging with near-infrared light: new technological advances that enable *in vivo* molecular imaging," European Radiology **13**, 195-208 (2003).
6. K. Konig, "Multiphoton microscopy in life sciences," Journal of Microscopy-Oxford **200**, 83-104 (2000).
7. J. G. Fujimoto, M. E. Brezinski, G. J. Tearney, S. A. Boppart, B. Bouma, M. R. Hee, J. F. Southern, and E. A. Swanson, "Optical biopsy and imaging using optical coherence tomography," Nature Medicine **1**, 970-972 (1995).
8. H. Sato, T. Suzuki, B. B. Andriana, S. Morita, A. Maruyama, H. Shinzawa, Y. Komachi, G. Kanai, N. Ura, K. Masutani, Y. Matsuura, M. Toi, T. Shimosegawa,

and Y. Ozaki, "An optical biopsy system with miniaturized raman and spectral imaging probes; *in vivo* animal and *ex vivo* clinical application studies," Proceedings of SPIE **7169,** (2009).

9. C. Piazza, F. Del Bon, G. Peretti, S. Mangili, A. Bizzoni, and P. Nicolai, ""Optical biopsy" by narrow band imaging and autofluorescence of oral and oropharyngeal erythro-leukoplakias," Lasers in Surgery and Medicine **44**, 22 (2012).

10. B. H. Li, and S. S. Xie, "Fluorescence spectroscopy and imaging for optical biopsy," Spectroscopy and Spectral Analysis **25**, 1083-1087 (2005).

11. I. Schneider, "Medical imaging - optical biopsy prescreens tissue at risk for cancer," Laser Focus World **43**, 46 (2007).

12. I. I. Smalyukh, S. V. Shiyanovskii, and O. D. Lavrentovich, "Three-dimensional imaging of orientational order by fluorescence confocal polarizing microscopy," Chemical Physics Letters **336**, 88-96 (2001).

13. P. Galli, G. Strona, A. M. Villa, F. Benzoni, S. Fabrizio, S. M. Doglia, and D. C. Kritsky, "Three-dimensional imaging of monogenoidean sclerites by laser scanning confocal fluorescence microscopy," Journal of Parasitology **92**, 395-399 (2006).

14. J. D. Bhawalkar, J. Swiatkiewicz, S. J. Pan, J. K. Samarabandu, W. S. Liou, G. S. He, R. Berezney, P. C. Cheng, and P. N. Prasad, "Three-dimensional laser scanning two-photon fluorescence confocal microscopy of polymer materials using a new, efficient upconverting fluorophore," Scanning **18**, 562-566 (1996).

15. B. R. Masters, P. T. C. So, and E. Gratton, "Multiphoton excitation microscopy of *in vivo* human skin - functional and morphological optical biopsy based on three-dimensional imaging, lifetime measurements and fluorescence spectroscopy," Advances in Optical Biopsy and Optical Mammography **838**, 58-67 (1998).

16. N. Safdarian, Z. Y. Liu, X. M. Zhou, H. Appelman, T. T. Nostrant, T. D. Wang, and E. T. Wang, "Quantifying human eosinophils using three-dimensional volumetric images collected with multiphoton fluorescence microscopy," Gastroenterology **142**, 15-24 (2012).

17. P. J. Campagnola, M. D. Wei, A. Lewis, and L. M. Loew, "High-resolution nonlinear optical imaging of live cells by second harmonic generation," Biophysical Journal **77**, 3341-3349 (1999).

18. D. Oron, D. Yelin, E. Tal, S. Raz, R. Fachima, and Y. Silberberg, "Depth-resolved structural imaging by third-harmonic generation microscopy," Journal of Structural Biology **147**, 3-11 (2004).

19. Y. Fu, H. Wang, R. Shi, and J. X. Cheng, "Second harmonic and sum frequency generation imaging of fibrous astroglial filaments in *ex vivo* spinal tissues," Biophysical Journal **92**, 3251-3259 (2007).

20. A. Zumbusch, G. R. Holtom, and X. S. Xie, "Three-dimensional vibrational imaging by coherent anti-stokes raman scattering," Physical Review Letters **82**, 4142-4145 (1999).

21. D. Fu, T. Ye, T. E. Matthews, B. J. Chen, G. Yurtserver, and W. S. Warren, "High-resolution *in vivo* imaging of blood vessels without labeling," Optics Letters **32**, 2641-2643 (2007).

22. D. Fu, T. Ye, T. E. Matthews, G. Yurtsever, and W. S. Warren, "Two-color, two-photon, and excited-state absorption microscopy," Journal of Biomedical Optics **12**, 054004 (2007).

23. G. Ku, X. Wang, X. Xie, G. Stoica, and L. V. Wang, "Imaging of tumor angiogenesis in rat brains *in vivo* by photoacoustic tomography," Applied Optics **44**, 770-775 (2005).

24. J. T. Oh, M. L. Li, H. F. Zhang, K. Maslov, G. Stoica, and L. H. V. Wang, "Three-dimensional imaging of skin melanoma in vivo by dual-wavelength photoacoustic microscopy," Journal of Biomedical Optics **11**, 034032 (2006).

25. D. K. Yao, K. Maslov, K. K. Shung, Q. Zhou, and L. V. Wang, "*In vivo* label-free photoacoustic microscopy of cell nuclei by excitation of DNA and RNA," Optics Letters **35**, 4139-4141 (2010).

26. Y. W. Wang, X. Y. Xie, X. D. Wang, G. Ku, K. L. Gill, D. P. O'neal, G. Stoica, and L. V. Wang, "Photoacoustic tomography of a nanoshell contrast agent in the *in vivo* rat brain," Nano Letters **4**, 1689-1692 (2004).

27. J. Yao, K. Maslov, S. Hu, and L. V. Wang, "Evans blue dye-enhanced capillary-resolution photoacoustic microscopy *in vivo*," Journal of Biomedical Optics **14**, 054049 (2009).

28. K. H. Song, and L. V. Wang, "Deep reflection-mode photoacoustic imaging of biological tissue," Journal of Biomedical Optics **12**, 060503 (2007).

29. K. Maslov, H. F. Zhang, S. Hu, and L. V. Wang, "Optical-resolution photoacoustic microscopy for in vivo imaging of single capillaries," Optics Letters **33**, 929-931 (2008).

30. C. M. W. Daft, G. A. D. Briggs, and W. D. Obrien, "Frequency-dependence of tissue attenuation measured by acoustic microscopy," Journal of the Acoustical Society of America **85**, 2194-2201 (1989).

31. T. E. Ustun, N. V. Iftimia, R. D. Ferguson, and D. X. Hammer, "Real-time processing for fourier domain optical coherence tomography using a field programmable gate array," Review of Scientific Instruments **79**, 114301 (2008).

32. R. A. Colyer, C. Lee, and E. Gratton, "A novel fluorescence lifetime imaging system that optimizes photon efficiency," Microscope Research and Technology **71**, 201-213 (2008).

33. D. S. Gareau, S. Abeytunge, and M. Rajadhyaksha, "Line-scanning reflectance confocal microscopy of human skin: comparison of full-pupil and divided-pupil configurations," Optics Letters **34**, 3235-3237 (2009).

34. J. A. Jensen, O. Holm, L. J. Jensen, H. Bendsen, S. I. Nikolov, B. G. Tomov, P. Munk, M. Hansen, K. Salomonsen, J. Hansen, K. Gormsen, H. M. Pedersen, and K. L. Gammelmark, "Ultrasound research scanner for real-time synthetic aperture data acquisition," IEEE Transactions on Ultrasonic and Ferroelectric Frequency Control **52**, 881-891 (2005).

35. S. Jie, X. Qin, L. Ying, and L. Gengying, "Home-built magnetic resonance imaging system (0.3 t) with a complete digital spectrometer," Review of Scientific Instruments **76**, 105101 (2005).

36. L. V. Wang and H. I. Wu, *Biomedical Optics: Principles and Imaging* (Wiley-Interscience, 2007).

37. H. F. Zhang, K. Maslov, G. Stoica, and L. H. V. Wang, "Imaging acute thermal burns by photoacoustic microscopy," Journal of Biomedical Optics **11**, 054032 (2006).

38. H. F. Zhang, K. Maslov, G. Stoica, and L. V. Wang, "Functional photoacoustic microscopy for high-resolution and noninvasive *in vivo* imaging," Nature Biotechnology **24**, 848-851 (2006).

39. M. L. Li, J. C. Wang, J. A. Schwartz, K. L. Gill-Sharp, G. Stoica, and L. V. Wang, "*In vivo* photoacoustic microscopy of nanoshell extravasation from solid tumor vasculature," Journal of Biomedical Optics **14**, 010507 (2009).

40. K. Maslov, G. Stoica, and L. V. H. Wang, "*In vivo* dark-field reflection-mode photoacoustic microscopy," Optics Letters **30**, 625-627 (2005).

41. Olympus NDT, "Ultrasonic transducers technical notes," http://www.olympus-ims.com/data/File/panametrics/UT-technotes.en.pdf.

42. R. J. Zemp, R. Bitton, M. L. Li, K. K. Shung, G. Stoica, and L. V. Wang, "Photoacoustic imaging of the microvasculature with a high-frequency ultrasound array transducer," Journal of Biomedical Optics **12**, 010501 (2007).

43. E. W. Stein, K. Maslov, and L. H. V. Wang, "Noninvasive, *in vivo* imaging of the mouse brain using photoacoustic microscopy," Journal of Applied Physics **105**, 102027 (2009).

44. Y. Wang, K. Maslov, Y. Zhang, S. Hu, L. Yang, Y. Xia, J. Liu, and L. V. Wang, "Fiber-laser-based photoacoustic microscopy and melanoma cell detection," Journal of Biomedical Optics **16**, 011014 (2011).

45. G. Ku, K. Maslov, L. Li, and L. H. V. Wang, "Photoacoustic microscopy with 2-mu m transverse resolution," Journal of Biomedical Optics **15**, 021302 (2010).

46. K. Maslov, G. Ku, and L. V. Wang, "Photoacoustic microscopy with submicron resolution," Proceedings of SPIE **7564**, (2010).

47. Z. Xie, S. Jiao, H. F. Zhang, and C. A. Puliafito, "Laser-scanning optical-resolution photoacoustic microscopy," Optics Letters **34**, 1771-1773 (2009).

48. W. Shi, S. Kerr, I. Utkin, J. Ranasinghesagara, L. Pan, Y. Godwal, R. J. Zemp, and R. Fedosejevs, "Optical resolution photoacoustic microscopy using novel high-repetition-rate passively q-switched microchip and fiber lasers," Journal of Biomedical Optics **15**, 056017 (2010).

49. M. Jiang, X. Zhang, C. A. Puliafito, H. F. Zhang, and S. Jiao, "Adaptive optics photoacoustic microscopy," Optics Express **18**, 21770-21776 (2010).

50. R. L. Shelton and B. E. Applegate, "Off-axis photoacoustic microscopy," IEEE Transactions on Biomedical Engineering **57**, 1835-1838 (2010).

51. G. York and Y. Kim, "Ultrasound processing and computing: review and future directions," Annual Review on Biomedical Engineering **1**, 559-588 (1999).

52. J. Gamelin, A. Aguirre, A. Maurudis, F. Huang, D. Castillo, L. V. Wang, and Q. Zhu, "Curved array photoacoustic tomographic system for small animal imaging," Journal of Biomedical Optics **13**, 024007 (2008).

53. R. A. Kruger, D. R. Reinecke, and G. A. Kruger, "Thermoacoustic computed tomography--technical considerations," Medical Physics **26**, 1832-1837 (1999).

54. J. H. Chang, J. T. Yen, and K. K. Shung, "A novel envelope detector for high-frame rate, high-frequency ultrasound imaging," IEEE Transactions on Ultrasonic and Ferroelectric Frequency Control **54**, 1792-1801 (2007).

55. B. G. Tomov, and J. A. Jensen, "Compact FPGA-based beamformer using oversampled 1-bit A/D converters," IEEE Transactions on Ultrasonic and Ferroelectric Frequency Control **52**, 870-880 (2005).

56. Y. S. Yang, S. Vaithilingam, H. T. J. Ma, S. Salehi-Had, O. Oralkan, B. T. Khuri-Yakub, and S. Guccione, "Development of nanoparticle-based gold contrast agent for photoacoustic tomography," Proceedings of NSTI Nanotech **1**, 708-711 (2008).

57. G. Kim, S. W. Huang, K. C. Day, M. O'donnell, R. R. Agayan, M. A. Day, R. Kopelman, and S. Ashkenazi, "Indocyanine-green-embedded pebbles as a contrast agent for photoacoustic imaging," Journal of Biomedical Optics **12**, 044020 (2007).

58. C. E. Crespo-Hernandez, B. Cohen, and B. Kohler, "Base stacking controls excited-state dynamics in a[middot]t DNA," Nature **436**, 1141 (2005).

59. B. E. Applegate and J. A. Izatt, "Molecular imaging of endogenous and exogenous molecular chromophores with ground state recovery pump-probe optical coherence tomography," Optics Express **14**, 9142-9155 (2006).

60. B. E. Applegate, C. Yang, and J. A. Izatt, "Theoretical comparison of the sensitivity of molecular contrast optical coherence tomography techniques," Optics Express **13**, 8146-8163 (2005).

61. C. Y. Dong, P. T. C. So, C. Buehler, and E. Gratton, "Spatial resolution in scanning pump-probe fluorescence microscopy," Optik **106**, 7-14 (1997).

62. C. J. R. Sheppard and M. Gu, "Image-formation in 2-photon fluorescence microscopy," Optik **86**, 104-106 (1990).

63. J. Squier and M. Muller, "High resolution nonlinear microscopy: A review of sources and methods for achieving optimal imaging," Review of Scientific Instruments **72**, 2855-2867 (2001).

64. C. Zhang, K. Maslov, and L. H. V. Wang, "Subwavelength-resolution photoacoustic microscopy for label-free detection of optical absorption *in vivo*," Proceedings of SPIE **7899,** (2011).

65. R. L. Shelton and B. E. Applegate, "Ultrahigh resolution photoacoustic microscopy via transient absorption," Biomedical Optics Express **1**, 676-686 (2010).

66. J. Mertz, C. Xu, and W. W. Webb, "Single-molecule detection by two-photon-excited fluorescence," Optics Letters **20**, 2532-2534 (1995).

67. S. Ashkenazi, S. W. Huang, T. Horvath, Y. E. L. Koo, and R. Kopelman, "Photoacoustic probing of fluorophore excited state lifetime with application to oxygen sensing," Journal of Biomedical Optics **13,** 034023 (2008).

68. S. Ashkenazi, "Photoacoustic lifetime imaging of dissolved oxygen using methylene blue," Journal of Biomedical Optics **15,** 040501 (2010).

69. Q. S. Hanley, V. Subramaniam, D. J. Arndt-Jovin, and T. M. Jovin, "Fluorescence lifetime imaging: multi-point calibration, minimum resolvable differences, and artifact suppression," Cytometry **43**, 248-260 (2001).

70. R. F. Kubin and A. N. Fletcher, "Fluorescence quantum yields of some rhodamine dyes," Journal of Luminescence **27**, 455-462 (1982).

71. K. B. Saebvarnothing, "Accurate de-oxygenation of ex vivo whole blood using sodium dithionite," Proceedings of the International Society for Magnetic Resonance Medicine **8,** 2025 (2000).

72. S. Q. Ye, R. Yang, J. W. Xiong, K. K. Shung, Q. F. Zhou, C. H. Li, and Q. S. Ren, "Label-free imaging of zebrafish larvae in vivo by photoacoustic microscopy," Biomedical Optics Express **3**, 360-365 (2012).

73. B. Rao, K. Maslov, A. Danielli, R. M. Chen, K. K. Shung, Q. F. Zhou, and L. V. Wang, "Real-time four-dimensional optical-resolution photoacoustic microscopy with AU nanoparticle-assisted subdiffraction-limit resolution," Optics Letters **36**, 1137-1139 (2011).

74. R. Huber, D. C. Adler, V. J. Srinivasan, and J. G. Fujimoto, "Fourier domain mode locking at 1050 nm for ultra-high-speed optical coherence tomography of

the human retina at 236,000 axial scans per second," Optics Letters **32**, 2049-2051 (2007).

75. K. Ohbayashi, D. Choi, H. Hiro-Oka, H. Furukawa, R. Yoshimura, M. Nakanishi, and K. Shimizu, "60 MHz A-line rate ultra-high speed fourier-domain optical coherence tomography," Proceedings of SPIE **6847**, (2008).

76. H. M. Subhash, L. An, and R. K. K. Wang, "Ultra-high speed full range complex spectral domain optical coherence tomography for volumetric imaging at 140,000 A-scans per second," Proceedings of SPIE **7554**, (2010).

77. L. An, P. Li, T. T. Shen, and R. K. Wang, "High speed spectral domain optical coherence tomography for retinal imaging at 500,000 A-lines per second," Biomedical Optics Express **2**, 2770-2783 (2011).

78. B. E. Applegate, C. Yang, J. A. Izatt, "Theoretical comparison of the sensitivity of molecular contrast optical coherence tomography techniques," Optics Express **13**, 8146-8163 (2005).

APPENDIX A

DERIVATION OF TAUM SIGNAL

This effort to fully derive the signal content existing in the transient absorption ultrasonic microscope closely follows the transient absorption derivation found in [78]. In order to properly define the expected photoacoustic signal and its frequency content, the excitation beams must be defined. While the pulsed light is better represented by a low duty cycle square wave, it is being represented as a cosine function for simplification purposes. This approximation will suffice to describe the origin of the signals and the resulting frequency content. The power of the probe beam, modulated by the repetition rate of the laser, is defined as

$$P_{pr} = \frac{P_{pr_0}}{2} \sum_{n=0}^{\infty} A_n \cos\left(2\pi f_{rep} n t\right), \tag{A.1}$$

where P_{pr_0} is the average power of the probe beam, A_n is the coefficient for the harmonic series, and f_{rep} is the repetition rate of the laser. For the purposes of this derivation, the series is truncated after the 2nd term, discarding the harmonic content to yield

$$P_{pr} = P_{pr_0}\left[\frac{1}{2} + \frac{1}{2}\cos\left(2\pi f_{rep} t\right)\right]. \tag{A.2}$$

Upon introducing the optical chopper, the probe power is given a carrier frequency, resulting in frequency mixing between the laser repetition rate and the chopping frequency:

$$P_{pr}{}' = P_{pr_0}\left[\frac{1}{2}+\frac{1}{2}\cos\left(2\pi f_{rep}t\right)\right]\cdot\left[\frac{1}{2}+\frac{1}{2}\cos\left(2\pi f_{pr}t\right)\right]$$
$$= \frac{P_{pr_0}}{4}\left[1+\cos\left(2\pi f_{pr}t\right)+\cos\left(2\pi f_{rep}t\right)+\frac{1}{2}\cos\left(2\pi\left(f_{rep}-f_{pr}\right)t\right)+\frac{1}{2}\cos\left(2\pi\left(f_{rep}+f_{pr}\right)t\right)\right], \quad \text{(A.3)}$$

where $P_{pr}{}'$ denotes the chopped probe power and f_{pr} is the chopping frequency of the probe beam. The chopped pump power is similarly derived:

$$P_{pu}{}' = \frac{P_{pu_0}}{4}\left[1+\cos\left(2\pi f_{pu}t\right)+\cos\left(2\pi f_{rep}t\right)+\frac{1}{2}\cos\left(2\pi\left(f_{rep}-f_{pu}\right)t\right)+\frac{1}{2}\cos\left(2\pi\left(f_{rep}+f_{pu}\right)t\right)\right], \quad \text{(A.4)}$$

where $P_{pu}{}'$ denotes the chopped pump power, P_{pu_0} is the average power of the pump beam, and f_{pu} is the chopping frequency of the pump beam.

Now that the pump and probe excitation has been defined, the signals generated from this excitation can be explored. The photoacoustic pressure rise in a spherical absorber resulting from the absorption of light is described as

$$p\left(r,t\right) = \frac{\mu_a \beta F {v_s}^2}{2C_p\left(r/a\right)}\left(1-\hat{\tau}\right)\hat{\Theta}\left(\hat{\tau}\right), \quad \text{(A.5)}$$

where $p\left(r,t\right)$ is the spatial and temporal-dependent pressure profile, r is the radial dimension, μ_a is the absorption coefficient, β is the expansion coefficient, F is the optical fluence, v_s is the speed of sound in the absorber, C_p is the specific heat, a is the radius of the absorber, $\hat{\tau}$ is the dimensionless time parameter, and $\Theta\left(\hat{\tau}\right)$ is the square wave function. For the purposes of this derivation, the important parameters are $p\left(r,t\right)$ μ_a, and F. The remaining terms will be grouped into a simplification term since they remain unchanged throughout the derivation. Additionally, multiplying by the area of

the incident light and the laser repetition rate, i.e. $\left(A \cdot f_0\right)$, converts the optical fluence to optical power. This simplification results in

$$p\left(r,t\right) = \left(\mu_a P_{pu}{}' + \mu_a{}' P_{pr}{}'\right)\Gamma\left(r,t\right), \tag{A.6}$$

where $\mu_a{}'$ denotes the population-dependent absorption coefficient after the pump has interacted with the absorber and $\Gamma\left(r,t\right) = \frac{\beta v_s{}^2 A f_0}{2C_p\left(r/a\right)}\left(1-\hat{\tau}\right)\Theta\left(\hat{\tau}\right)$ is the simplification term. It is important to note that due to the line shape of a photoacoustic pulse, the resulting frequency spectrum of the photoacoustic signal is very broadband. As a result, a very large number of harmonics from the 10 kHz repetition rate are generated; these harmonics are integrated across the transducer bandwidth to form the TAUM signal. The extra term in (A.6) is due to the fact that two consecutive pulses are generating the pressure rise in each pulse sequence, one pulse from the pump beam and one pulse from the probe beam. The population-dependent absorption coefficient is given by

$$\mu_a{}' = N_1\left(t\right)\sigma, \tag{A.7}$$

where $N_1\left(t\right)$ is the population of the ground state and σ is the absorption cross-section of the chromophore. For clarity, the pump interaction is restricted to a 2-level system, with populations of N_1 and N_2. Assuming state 2 is unpopulated before pump interaction occurs; the time-dependent populations may be defined as

$$N_1\left(t\right) = \frac{N_1{}^0}{2\rho B + A}\left[A + \rho B + \rho B \exp\left(-\left(2\rho B + A\right)t\right)\right] \tag{A.8}$$

$$N_2(t) = N_1^0 - N_1 = \frac{\rho B N_1^0}{2\rho B + A}\left[1 - \exp\left(-\left(2\rho B + A\right)t\right)\right], \tag{A.9}$$

where N_1^0 is the initial population of state 1, ρ is the radiation density, and A and B are Einstein coefficients.

Under the assumption that the absorption coefficient is constant over the pump bandwidth (a fair assumption, given the narrow bandwidth of the Q-switched laser), the following approximation holds true:

$$\rho B = \frac{\sigma \lambda_{pu} P_{pu}'}{hc\pi\omega_0^2}, \tag{A.10}$$

where λ_{pu} is the pump wavelength, h is Planck's constant, c is the speed of light, and ω_0 is the radius of the focal spot.

Since these experiments concern single pulse interactions, the population equations must be derived for a single pulse. This is easily achieved by multiplying (A.8) and (A.9) by (τf_0), where τ is the pulse duration and f_0 is the laser repetition rate. This is accurate under the assumption that the ground state is repopulated after each pulse, i.e. $A >> f_0$. Since these experiments use a relatively low repetition rate (10 kHz), this is a fair assumption. Einstein coefficient A is assumed to be zero (i.e. $A << 1/\tau$). This assumption is used to simplify the derivation. The relevant lifetimes in the experiment are on the order of 10 ns, while the pulse duration is 1 ns; therefore, there will be a small change in the population over the pulse duration, but the intention of this derivation is to highlight the physical processes present in the work, and this assumption

will not change the information the derivation is intended to convey. Finally, the exponential functions in (A.8) and (A.9) are approximated by taking the Taylor series expansion and truncating after the second term. This is a common approximation, assuming that the light is only weakly absorbed, i.e. the transition is far from saturation. Rewriting the population equations in terms of pulse duration and applying the aforementioned assumptions yields

$$N_1 = N_1^0\left(1-\frac{\sigma\lambda_{pu}P'_{pu}}{hc\pi\omega_0^2 f_0}\right) \tag{A.11}$$

$$N_2 = N_1^0\frac{\sigma\lambda_{pu}P'_{pu}}{hc\pi\omega_0^2 f_0} \tag{A.12}$$

Inserting (A.11) into (A.7) gives the pump-dependent absorption coefficient,

$$\mu_a' = N_1\sigma = N_1^0\sigma\left(1-\frac{\sigma\lambda_{pu}}{hc\pi\omega_0^2 f_0}P_{pu}\right). \tag{A.13}$$

Inserting (A.13) into (A.6) gives the photoacoustic pressure rise in terms of the pump and probe power, i.e.:

$$p(r,t) = \left[\mu_a P_{pu}{}' + N_1{}^0\sigma\left(1-\frac{\sigma\lambda_{pu}}{hc\pi\omega_0{}^2 f_0}P_{pu}{}'\right)\cdot P_{pr}{}'\right]\Gamma(r,t). \tag{A.14}$$

Now that the modulated pump and probe beams have been defined, along with the photoacoustic pressure rise in terms of the modulated pump and probe power, the resulting signal and its frequency content may be investigated. Substituting (A.3) and (A.4) into (A.14) and expanding the products of the terms gives the frequency components of the resulting TAUM signal. Negative frequencies have been discarded,

assuming $f_{rep} > \left(f_{pu} + f_{pr}\right) > f_{pu} > f_{pr}$, which is the case for these experiments. Likewise, frequencies with negligible contribution over the transducer bandwidth and harmonics (which have already been implied) have also been discarded. In order to display the frequency content of the TAUM signal in a coherent fashion, the result of expanding (A.14) is presented in the frequency domain. The photoacoustic pressure rise induced by the pump and probe, modulated by the dual frequency chopper can be separated into three sets of frequencies: 1) PA fundamental, 2) PA single photon (pump and probe sidebands), and 3) PA two-photon (TAUM). The PA fundamental set is the strongest signal, consisting of PA signal at the repetition rate of the laser. This includes 10 kHz and its harmonics. The PA single photon set includes all other single photon frequency components, for instance, individual contributions from the pump beam and probe beam. The PA two photon set includes all of the pump-probe interaction signals. The sum of this last set determines the TAUM signal strength. The following equations detail the frequency components of each set of frequencies listed above, whose sum constitutes the complete PA signal, i.e.

$$p(\omega) = p_1(\omega) + p_2(\omega) + p_3(\omega) \tag{A.15}$$

$$p_1(\omega) = \frac{2\mu_a\left(P_{pu_0} + P_{pr_0}\right) + P_{pu_0}P_{pr_0}}{8}\delta\left(\omega_{rep}\right)\Gamma(\omega) \tag{A.16}$$

$$p_2(\omega) = \left[\frac{P_{pu_0}\left(2\mu_a + P_{pr_0}\right)}{16}\delta\left(\omega_{rep} \pm \omega_{pu}\right) + \frac{P_{pr_0}\left(2\mu_a + P_{pu_0}\right)}{16}\delta\left(\omega_{rep} \pm \omega_{pr}\right)\right]\Gamma(\omega) \tag{A.17}$$

$$p_3(\omega) = \frac{P_{pu_0}P_{pr_0}}{32}\delta\left(\omega_{rep} \pm \left(\omega_{pu} \pm \omega_{pr}\right)\right)\Gamma(\omega) \tag{A.18}$$

The TAUM signal is extracted by filtering around the 4 frequency bands contained in $p_3(\omega)$ and integrating the resulting signal.